



**BILINGUAL
PUBLISHING CO.**
Pioneer of Global Academics Since 1984

Journal of Metallic Material Research

Volume 4 · Issue 1 · April 2021 | ISSN 2630-5135 (Online)





**BILINGUAL
PUBLISHING CO.**
Pioneer of Global Academics Since 1984

Editor-in-Chief

Dr. Oleg Valentinovich

Sobol, Ukraine

Editorial Board Members

Shuo Chen, United States	Alexander Evgenievich Barmin, Ukraine
Changrui Wang, China	Khitam Abdulhussein Saeed, Malaysia
Recep Karadag, Turkey	Sertan Ozan, Turkey
Madhukar Eknath Navgire, India	Anand Krishnan, South Africa
Unal Camdali, Turkey	Farshad Darab-Golestan, Iran
Jitendra Kumar Singh, Korea	Mohammadreza Elahifard, Iran
Abhay Nanda Srivastva, India	Paparao Mondhi, India
Vivek Patel, India	Zbigniew Ranachowski, Poland
Aybaba Hançerlioğullari, Turkey	Sami ullah Rather, Saudi Arabia
Bandar Abdulaziz AlMangour, Saudi Arabia	Nickolaj Nikolayevich Rulyov, Ukraine
Soumen Maiti, India	Oğuzhan Keleştemur, Turkey
Jonathan David Parker, Canada	Shengqiang Ma, China
Jingyuan Yan, United States	Md Saiful Islam, Bangladesh
Satyanarayana Sirasani, India	Ajay Kumar Choubey, India
Xiaoan Hu, China	Saeed Kakaei, Iran
Derya Dispinar, Turkey	Hojat Jafari, Iran
Samson jerold samuel Chelladurai, India	Yuhan Liang, United States
Akash Deep Sharma, India	Ahmed Wagih, Egypt
Dan Dobrotă, Romania	Bhanodaya Kiran Babu Nadikudi, India
Asit Kumar Gain, Australia	Rong Liu, Canada
Dragica Milan Minic, Serbia	Mahmoud Pakshir, Iran
Zabiollah Mahdaviifar, Iran	Changhai Zhou, China
Chandan Pandey, India	Vishal Ishvarbhai Lad, United States
Mahnaz Mahdavi Shahri, Iran	Hossein Ghasemi Mobtaker, Iran
Janarthanan Gopalakrishnan, India	Francesco Caridi, Italy
Deniz Uçar, Turkey	Konstanti Viktorovich Ivanov, Russian Federation
Weidong Song, China	Dipak Kumar, India
Attoui Aissa, Algeria	Americo Scotti, Brazil
Mohammad Farnush, Iran	Ziad Salem Abu-Hamatteh, Jordan
Qiaoli Lin, China	Mohsen Vafaeifard, Malaysia
Hajar Zarei Se Dehi Zadeh, Iran	Hülya - Demirören, Turkey
Subravel Visvalingam, India	Tahir Mohiuddin Bhat, India
Asaminew Abiyu Cherinet, Ethiopia	Hamit Özkan Gülsoy, Turkey
Arif Gök, Turkey	Sandhya Dwevedi, India
Ning Li, China	Sergey Nikolaevich Lezhnev, Kazakhstan
Fufa Wu, China	Faysal Favez Eliyan, Canada
Wenchun Jiang, China	Shouxun Ji, United Kingdom
Saeed Zeinali Heris, Iran	Patrice Berthod, France
Himadri Bhusan Sahoo, India	Moslem Mansour Lakouraj, Iran
Vladimir Victorovich Lukov, Russian Federation	Akhyar - Akhyar, Indonesia
Abhishek Ghosh, India	Chih-Chun Hsieh, Taiwan
KangHua Chen, China	Recep Sadeler, Turkey
Pradeep L Menezes, United States	Lutfiddin Omanivich Olimov, Uzbekistan
Shuhua Zhang, China	Mahmoud Ebrahimi, Iran
Naushad Ahmad, India	Lineker Max Goulart Coelho, Brazil
S Selvam, India	Aslıhan Katip, Turkey
Guocheng Zhu, China	Serkan Islak, Turkey
Mohamed Kamal ElFawkhry, India	Murat Sarıkaya, Turkey
Mohammad Hassan Shirani Bidabadi, China	Yaofeng Chang, United States
Mohd Azli Salim, Malaysia	Mehmet Kaya, Turkey
Vladimir Mikhailov Yegorovich, Russian Federation	Yahya Absalan, Russian Federation
Kaveh Sheikhi Moghaddam, Iran	Xiang Wang, China
Robin Gupta, India	Meilinda Nurbanasari, Indonesia
Sergey Vasilevich Byvaltsev, Russian Federation	Rizk Mostafa Shalaby, Egypt
Nitin Saini, India	Anatolii Michailovich Lepikhin, Russian Federation
Ramesh Balakrishnan, India	

Volume 4 Issue 1 • April 2021 • ISSN 2630-5135 (Online)

Journal of Metallic Material Research

Editor-in-Chief

Dr. Oleg Valentinovich



**BILINGUAL
PUBLISHING CO.**
Pioneer of Global Academics Since 1984



Contents

Articles

- 1 L-Proline as a Green Corrosion Inhibitor in Aqueous Solutions for Carbon Steel**
Nisreen Faraj Kareima A. Abdelghani A.A. Idress Dalal. M. Ibrahim
- 6 Wetting of Laser Textured Cu Surface by Ethylene Glycol and Sn**
Kaibin Xie Yujie Ge Qiaoli Lin
- 12 Identification of an Appropriate Formulation for Domestic Water Ceramic Filters from Soukamna Clay (Cameroon)**
Ngiongbound Nguiamba Celestine Asobo Yanu Placide Désiré Belibi Belibi Joseph Marie Sieliechi Martin Benoît Ngassoum
- 19 A Constitutive Modeling and Experimental Effect of Shock Wave on the Microstructural Sub-strengthening of Granular Copper**
A. D. Sharma A. K. Sharma N. Thakur
- 26 Orange Peel Extract Mediated Silver Nanofluid as Corrosion Inhibitor for X80 Steel in Simulated Oilfield Scale Dissolver**
Ekemini Ituen Chukwudurom Dim Ekerete BoEKOM

Copyright

Journal of Metallic Material Research is licensed under a Creative Commons-Non-Commercial 4.0 International Copyright (CC BY- NC4.0). Readers shall have the right to copy and distribute articles in this journal in any form in any medium, and may also modify, convert or create on the basis of articles. In sharing and using articles in this journal, the user must indicate the author and source, and mark the changes made in articles. Copyright © BILINGUAL PUBLISHING CO. All Rights Reserved.

ARTICLE

L-Proline as a Green Corrosion Inhibitor in Aqueous Solutions for Carbon Steel

Nisreen Faraj Kareima A. Abdelghani A.A. Idress* Dalal. M. Ibrahim

Department of Chemistry, Faculty of Science, Omar Al Mukhtar University, Albayda, Libya

ARTICLE INFO

Article history

Received: 19 April 2021

Accepted: 10 June 2021

Published Online: 1 July 2021

Keywords:

Corrosion inhibition

Carbon steel

Proline

HCl

ABSTRACT

The chemical technique was used to investigate the inhibition and adsorption properties of L-proline for steel corrosion (weight loss method). As the concentration of L-proline increased, the inhibition efficiency increased, but decreased as the temperature increased, according to the findings. The inhibitor's adsorption to the steel surface has been shown to be random, involving both electrostatic and chemisorptions. The Temkin adsorption isotherm governs the adsorption of L-proline to the steel surface. Thermodynamic parameters have been determined in some cases.

1. Introduction

Corrosion protection is important in the petroleum industry because carbon steel is commonly used, such as in the construction of oil and gas production pipelines and transmission lines^[1].

Corrosion cells form on metal surfaces in contact with an electrolyte due to energy differences between the metal and the electrolyte. In relation to the electrolyte, different potentials can exist between different zones of the metal surface^[2]. The contents of the cell are as follows:

(1) A loaded anode zone is one of the first things you'll notice. The iron is oxidized in the anode zone.

(2) The cathode is loaded. Electrons are found in the cathode zone. These electrons are capable of reacting with other compounds.

(3) A metal path that allows electrons to pass through.

(4) An electrolyte that coats the iron's surface.

Because of its adsorption at the metal/solution

interface, this compound acts as an inhibitor. Adsorption is influenced by the inhibitor community's physicochemical properties^[3]. The existence of heteroatoms like N, O, and multiple bonds in its molecular structure, as well as functional and aromatic groups, donor atoms' electron density and p-orbital character, are thought to allow electrons to pass through adsorption centers^[4]. The toxicity of most corrosion inhibitors, on the other hand, which are toxic to living organisms and should therefore pollute the ecosystem, prompted us to look for environmentally friendly inhibitors^[5,6]. Heterocyclic compounds with π bonds, such as sulfur, oxygen, and nitrogen, are inhibitors^[7]. Functional groups, steric influences, electron density at the donor atom, and molecule electronic structure are all responsible for the physical properties of inhibitor molecules^[8,9]. The inhibitor can adsorb to the metal surface through two types of reactions. Physical adsorption is the electrostatic force between the absorbed species' ionic or dipolar

*Corresponding Author:

A.A. Idress,

Department of Chemistry, Faculty of Science, Omar Al Mukhtar University, Albayda, Libya;

Email: asma.alsalai@omu.edu.ly

charges and the electrical charge at the metal/solution interface. Chemical adsorption, on the other hand, occurs when charge from inhibitory molecules is shared or transferred to the metal surface, resulting in coordinated forms of bonds ^[10].

Proline is one of the twenty amino acids found in living organisms that make up their protein building blocks. Since the IUPAC meaning of an imine includes a carbon-nitrogen covalent bond, proline is commonly referred to as an imino acid. Proline is an aminoalkanoic acid that can be synthesized from glutamine. The aim of this study is to evaluate the corrosion inhibition of carbon steel in 1M HCl in the presence of various concentrations of L-proline using the weight loss technique at 298-328K, as well as to measure and discuss the thermodynamic functions for the dissolution and adsorption processes. It was selected as an inhibitor based on molecular structure considerations because it is an organic compound with many adsorption centers.

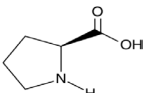
2. Experimental

2.1 Materials

Carbon steel specimens with the following compositions (percent by weight) were used in the tests: 0.200 C, 0.350 Mn, 0.014 P, and 0.003 S.

2.2 Inhibitors

Table 1. the molecular structure of L-proline as well as other data.

Structure	Mol. formula	Mol.wt.
	C ₅ H ₉ NO ₂	115.13 g mol ⁻¹

2.3 Solutions

Analytical grade HCl (37 percent) was diluted with double distilled water to make 1M HCl solutions. The inhibitors were used at various concentrations ranging from 2 X10⁻³ to 8 X 10⁻³ M.

2.4 Weight Loss Measures

In a thermostatically regulated water bath, weight loss measurements were taken in a 100 mL glass beaker. The length of the answer was 50 milliliters. Oblong steel coupons (2 cm long, 2 cm wide, 0.2 cm thick) were used. Before all of the tests, the coupons were polished with metallographic sandpaper with an accelerated fineness of

up to 1200 grains. After that, the electrode was washed twice in water, degreased with acetone, washed twice more in water, and dried at room temperature with a towel. The samples were weighed and suspended for 3 hours at (25-55 °C) in 50 ml of a 1.0 M HCl solution containing L-proline at the necessary concentrations. The coupons were washed in water, degreased with ethanol, washed again in water, dried, and weighed on an analytical balance after the tests were completed (precision: 0.1 mg). The inhibition efficiency (percent IE) was estimated using the equation below overtime periods of exposure:

$$\% IE = \theta \times 100 = \left(1 - \frac{W_{(inh)}}{W_{(free)}} \right) \times 100 \quad (1)$$

The weight loss in the absence and presence of the inhibitor is represented by surface coverage and W(free), W(inh).

3. Results and Discussion

3.1 Effect of Concentration

Table 2 shows the difference in weight loss of steel in the presence of varying concentrations (2x10⁻³ - 8x10⁻³ M) of L-proline in 1 M HCl for 3.0 h at 25 °C. They were plotted out. Figure 1 shows that L-proline inhibits steel corrosion in a 1 M HCl solution at the lowest concentrations used in the analysis, with the highest inhibition efficiency seen at an inhibitor concentration of 8 x 10⁻³ M in 1 M HCl at 25 °C. The addition of L-proline reduces the rate of corrosion, as shown in Table 2. The linear change in weight loss over time in uninhibited and inhibited 1 M HCl indicates the absence of insoluble surface films throughout corrosion. This may be because the adsorption of inhibitor molecules on the surface of carbon steel increases with increasing inhibitor concentration, effectively separating the carbon steel surface from the medium ^[11,12].

Table 2. Corrosion rate (C.R.) and inhibition efficiency data for carbon steel in 1 M HCl solutions without and with various concentrations of L-proline at 25 1°C derived from weight loss measurements.

Conc.,M	C.R., mg cm ⁻² min ⁻¹	θ	% IE
1 M HNO ₃	2.68	-	-
2x10 ⁻³ M	0.80	0.690	69.0
4x10 ⁻³ M	0.56	0.791	79.1
6x10 ⁻³ M	0.39	0.832	83.2
8x10 ⁻³ M	0.35	0.862	86.2

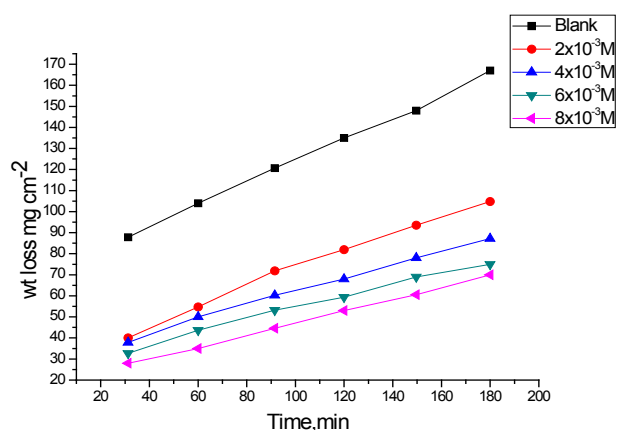


Figure 1. Weight loss-time curves of carbon steel in 1 M HCl in the absence and presence of different concentrations of L-proline at 25°C.

3.2 Effect of Temperature

Weight loss measurements were used to investigate the impact of temperature on both the corrosion rate and thus the inhibition efficiency of L-proline in each of 1M HCL within the range of 25-55°C with a 10°C increment, Table 3 shows that increasing the temperature causes an increase in steel corrosion rate in both free and inhibited acid solutions, as well as a decrease in L-proline inhibition efficiency, assuming that the test compound prevents steel corrosion by adsorbing an inhibitor molecule, while the test compound desorbs at higher temperatures [13].

The apparent energy of activation (E_a^*), activation enthalpy (ΔH^*), and activation entropy (ΔS^*) for steel corrosion in 1 M HCl solution were calculated using the Arrhenius form equation in the absence and presence of various concentrations of L-proline [14].

$$\text{Rate}(k) = A e^{\frac{-E_a^*}{RT}} \quad (2)$$

and transition state equation [15].

$$\text{Rate}(k) = \frac{RT}{Nh} e^{\frac{\Delta S^*}{R}} e^{\frac{-\Delta H^*}{RT}} \quad (3)$$

Where the frequency factor is (A), the Planck constant is (h), the Avogadro number is (N), and the universal gas constant is (R).

The kinetic parameters obtained from log Rate vs. ($1/T$) (Figure 2) are mentioned in Table 4 and ($1/T$) vs. log (Rate / T) (See Figure 3) showed that the value of E_a^* in an inhibited solution is higher than in an uninhibited solution, meaning that steel dissolution is slow in the presence of an inhibitor, which can be clarified by physical adsorption [16]. Equation 2 indicates that the higher the E_a^* value, the less the corrosion risk is. That is frequently way to the advent of a film at the metallic surface, which acts as a strength buffer in opposition to

Table 3. Weight loss measurements for carbon steel in 1 M HCl solution in the absence and presence of different L-proline concentrations at 25–55°C±1°C.

Conc.	Temp., °C	C.R., mg cm ⁻² min ⁻¹	θ	% IE
2x10 ⁻³ M	25	2.68	0.205	69.0
	35	2.88	0.109	10.9
	45	3.61	0.089	8.9
	55	9.63	0.054	5.4
4x10 ⁻³ M	25	0.80	0.726	79.1
	35	2.01	0.529	52.9
	45	2.87	0.328	32.8
	55	7.33	0.225	22.5
6x10 ⁻³ M	25	0.56	0.819	83.9
	35	1.91	0.709	70.2
	45	1.10	0.543	54.3
	55	5.34	0.482	48.2
8x10 ⁻³ M	25	0.35	0.873	86.2
	35	1.98	0.834	83.4
	45	4.82	0.718	71.8
	55	4.45	0.669	66.9

metallic corrosion [17]. Positive ΔH^* values indicate that the steel dissolution process is endothermic. The high and negative values of ΔS^* indicate that the active compound in the rate-determining phase is an interaction rather than a dissociation, implying that when the reactants and active compound are switched, the perturbation decreases [18].

Table 4. Effect of concentration of L-proline on the activation energy of carbon steel dissolution in 1 M HCl.

Conc. M	Activation parameters		
	E_a^* kJ mol ⁻¹	ΔH^* kJ mol ⁻¹	$-\Delta S^*$ J mol ⁻¹ K ⁻¹
1 M HCl ₃	23.60	21.20	198.9
2x10 ⁻³ M	40.12	41.52	153.50
4x10 ⁻³ M	47.20	45.44	141.23
6x10 ⁻³ M	65.9	57.34	135.12
8x10 ⁻³ M	89.12	61.96	99.65

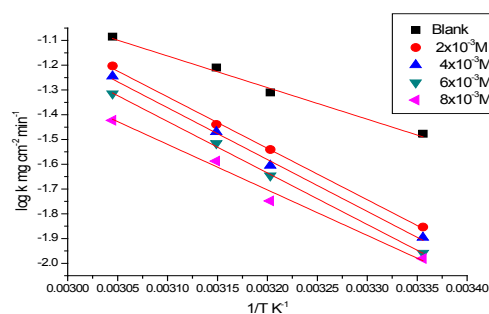


Figure 2. log corrosion rate vs $1/T$ curves for carbon steel dissolution in 1M HCl in absence and presence of different concentrations of L-proline.

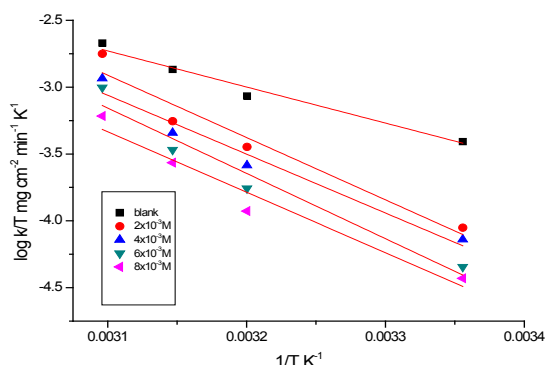


Figure 3. log corrosion rate/T vs 1/T curves for carbon steel dissolution in 1M HCl in absence and presence of different concentrations of L-proline.

3.3 Adsorption Isotherm Behavior

The following equation was used to calculate the values of surface coverage for various inhibitor concentrations in 1 M HCl based on weight loss measurements:

$$\theta = \frac{[\text{weight loss}(\text{pure}) - \text{weight loss}(\text{inh.})]}{\text{weight loss}(\text{pure})} \quad (4)$$

The values of θ increased as the inhibitor concentration increased, as can be seen from the values of θ . Using these surface coverage values, different adsorption isotherms can be used to process the experimental results.

It can be seen from the values of θ that the values of θ increased as the inhibitor concentration increased. Different adsorption isotherms may be used to process the experimental data using these surface coverage values. To investigate the adsorption mechanism, the adsorption mechanism was studied using the Temkin adsorption isotherm. The isotherm is defined by the equation below.

$$\ln K_{\text{ads}} C = a \theta \quad (5)$$

K_{ads} is the adsorption constant, and C is the inhibitor concentration. The plot of θ versus $\log C$ gives linear relation (shown in Figure 4). The adsorption constant K_{ads} are often calculated from the intercept and $\Delta G^{\circ}_{\text{ads}}$ are often calculated from the subsequent equation:

$$K_{\text{ads}} = 1/55.5 \exp (\Delta G^{\circ}_{\text{ads}}/RT) \quad (6)$$

Where 55.5 represents the mole/liter concentration of water in solution^[19], T is the absolute temperature, and R is the universal gas constant.

The thermodynamic parameters for the adsorption process derived from Figure 4 are shown in Table 5. The increased inhibition efficiency and negative G°_{ads} values indicate that the investigated compound is strongly adsorbed on the metal's surface, and the spontaneity adsorption mechanism aids in the creation of a stable adsorption layer on the metal's surface.

$\Delta G^{\circ}_{\text{ads}}$ up to -20 kJ mol^{-1} are based on the electrostatic interaction between charged molecules, and thus the charged metal (physical adsorption). $\Delta G^{\circ}_{\text{ads}}$ less than -40 kJ mol^{-1} involve the exchange or transfer of electrons from inhibitor molecules to the metal surface to form a coordinate bond (chemisorption)^[20]. The obtained $\Delta G^{\circ}_{\text{ads}}$ values were approximately equivalent to -59 kJ mol^{-1} , indicating that both electrostatic and chemisorption processes are involved in inhibitor molecule adsorption on carbon steel in 1 M HCl solution^[21]. The thermodynamic parameters relate to the inhibitors' decomposition (primary contributor) and chemical tests (secondary contributor) on the metal surface. K_{ads} follows a similar pattern, with higher values indicating more effective absorption and, as a result, better inhibition efficiency^[22].

Table 5. the inhibitor binding constant (K_{ads}), free energy of binding ($\Delta G^{\circ}_{\text{ads}}$), and later interaction parameter (a) for the corrosion of carbon steel in 1 M HCl at 25°C for various inhibitor concentrations.

Conc. M	Temkin		
	a	$K_{\text{ads}} \times 10^{-8} \text{ mol L}^{-1}$	$\Delta G^{\circ}_{\text{ads}} \text{ kJ mol}^{-1}$
$2 \times 10^{-3} \text{ M}$	11.2	5.15	-58.9
$4 \times 10^{-3} \text{ M}$	10.8	3.38	-57.4
$6 \times 10^{-3} \text{ M}$	10.4	2.33	-55.8
$8 \times 10^{-3} \text{ M}$	10.1	1.65	-53.9

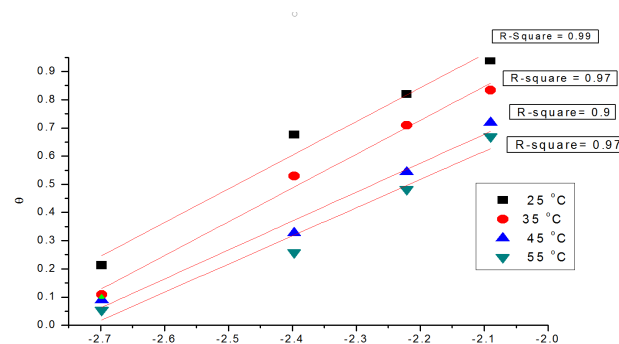


Figure 4. Temkin adsorption isotherm for carbon steel corrosion in 1 M HCl solutions at 25°C plotted as vs log C of L-proline.

4. Conclusions

The main assumptions are as follows:

- (1) L-proline has a significant inhibitory impact on steel corrosion in 1 M HCl.
- (2) As the inhibitor concentration rises, the value of inhibition efficiency falls, and as the temperature rises, the value of inhibition efficiency falls.
- (3) The Temkin adsorption isotherm governs the adsorption of L-proline on steel.

(4) The fact that the adsorption free energy was negative suggests that the reaction was exothermic and spontaneous.

References

- [1] M. Farsak, H. Keleş, and M. Keleş, "A new corrosion inhibitor for protection of low carbon steel in HCl solution," *Corrosion Science*, vol. 98, pp. 223-232, Sep 2015.
- [2] E., Bayol, K. Kayakirilmaz, and M. Erbil, "The inhibitive effect of hexamethylenetetramine on the acid corrosion of steel," *Mater.Chem.Phys.*, vol. 104, pp.74, Jul. 2007.
- [3] M. Bentiss, M. Traisnel, and M. Lagrenee, "Influence of 2, 5-bis (4 Dimethylaminophenyl)- 1, 3, 4- Thiadiazole on Corrosion Inhibition of Mild Steel in Acidic Media," *Journal of Applied Electrochemistry*, vol. 31, pp. 41–50, Jan. 2001.
- [4] A. S. Mahdi, "Amoxicillin as green corrosion inhibitor for concrete reinforced steel in simulated concrete pore solution containing chloride," *IJARET*, vol. 5, pp 99- 107, Jul. 2014.
- [5] A. A. Idress, and Dalal Ibrahim, "Inhibition Effect of Benzylpenicillin Drug Towards Corrosion of Carbon Steel in Acidic Solutions", May 2020.
- [6] R. K. Pathak, and P. Mishra, "Drugs as corrosion inhibitors: A review," *International Journal of Science and Research*, vol. 5, pp. 671- 677, Apr. 2016.
- [7] El-Naggar M.M., Corrosion Inhibition of Mild steel in Acidic Medium by some Sulfa Drugs Compounds, *Corrosion Science*, 49(5),2226-2236, 2007.
- [8] F. Zucchi, G. TrabANELLI, C. Monticelli, Inhibition of copper corrosion in aerated hydrochloric acid solution by amino-acid compounds, *Corros. Sci.* 38, 147,1996.
- [9] A. A. Idress, A. S. Fouda, K. Shalabi, The inhibition effect of Pistacia Atlantica towards the corrosion of copper and α -Brass in acidic solutions, second libyan conference on chemistry and its applications,9-11 may 2017, Binghazi.
- [10] Obot I.B., Obi-Egbedi N.O. and Umoren S.A. 2009. Adsorption Characteristics and Corrosion Inhibitive Properties of Clotrimazole for Aluminium Corrosion in Hydrochloric Acid. *International Journal of Electrochemical Science*.4:863-877.
- [11] Handbook of Corrosion Engineering, New York: McGraw Hill, Pierre R. Roberge, 1999, PP. 833-860.
- [12] A. S. Fouda, K. Shalabi , and A. A. Idress, "Ceratonia siliqua extract as a green corrosion inhibitor for copper and brass in nitric acid solutions," *Green Chemistry Letters and Reviews*, vol. 8, pp. 17-29, Oct. 2015.
- [13] H. M. Abd. El- Lateef, M. A. Abo-Riya, and A. H. Tantawy, "Empirical and quantum chemical studies on the corrosion inhibition performance of some novel synthesized cationic gemini surfactants on carbon steel pipelines in acid pickling processes," *Corrosion Science*, vol. 108, pp. 94-110, Jul. 2016.
- [14] Y. M. Abdallah and K. Shalabi, "Comprehensive study of the behavior of copper inhibition in 1 M HNO₃ by Euphorbia Helioscopia linn. extract as green inhibitor," *Protection of Metals and Physical Chemistry of Surfaces*, vol. 51(2), pp. 275-284, Mar. 2015.
- [15] .M. Samy Shaban, "N-(3-(Dimethyl benzyl ammonio) propyl) alkanamide chloride derivatives as corrosion inhibitors for mild steel in 1 M HCl solution: Experimental and theoretical investigation," *RSC Advances*, vol. 6, pp. 39784-39800, Apr. 2016.
- [16] S. Ghareba, S. Omanovic, "Interaction of 12-amino-dodecanoic acid with a carbon steel surface: Towards the development of 'green' corrosion inhibitors," *Corrosion Science* , vol. 52, pp. 2104-2113, Jun. 2010.
- [17] I. N. Putilova, S. A. Balezin, and V. P. Barannik, *Metallic Corrosion Inhibitors*, Pergamon Press, New York, London, 1960, p. 85.
- [18] A. Khadraouil, A. Khelifa1, H. Boutoumi1, et al., "Adsorption and Inhibitive Properties of Ruta chalepensis L. Oil as a Green Inhibitor of Steel in 1 M Hydrochloric Acid Medium," *Int. J. Electrochem. Sci.*, vol. 9, pp. 3334-3348, Mar. 2014.
- [19] E. M. Sherif, and S. Park, "Inhibition of copper corrosion in acidic pickling solutions by N-phenyl-1,4-phenylenediamine, " *Electrochim. Acta*, vol. 51, pp. 4665, Jun. 2006.
- [20] A. M. Eldesoky, Hala. M. Hassan, and A. S. Fouda, "Studies on the Corrosion Inhibition of Copper in Nitric Acid Solution Using Some Pharmaceutical Compounds," *Int. J. Electrochem. Sci.*, vol. 8, pp. 10376-10395, Aug. 2013.
- [21] S.Kertit , H. Essoufi , B.Hammouti , Benkaddour, 1 -phenyl-5-mercapto-1,2,3,4-tétrazole (PMT) : un nouvel inhibiteur de corrosion de l'alliage Cu-Zn efficace à très faible concentration. *M. Chim. Phys.* 95, 2070–2082, 1998.
- [22] E.M. Sherif , S. Park, Inhibition of copper corrosion in acidic pickling solutions by N-phenyl-1,4-phenylenediamine. *Electrochim. Acta*, 51, 4665, 2006.
- [23] Matos, J.B., Pereira, L.P., Agostinho, S.M.L., Barcia, O.E., Cordeiro, G.G.O., Elia E.D., (2004) . Effect of cysteine on the anodic dissolution of copper in sulfuric acid medium, *Electroanal. Chem.*, 570, 91.

ARTICLE**Wetting of Laser Textured Cu Surface by Ethylene Glycol and Sn****Kaibin Xie Yujie Ge Qiaoli Lin***

State Key Laboratory of Advanced Processing and Recycling of Non-ferrous Metal, Lanzhou University of Technology, Lanzhou, 730050, China

ARTICLE INFO*Article history*

Received: 3 July 2021

Accepted: 15 July 2021

Published Online: 20 July 2021

Keywords:

Wettability

Nanosecond laser

Roughness

Soldering

Texturing

ABSTRACT

The effect of microcosmic morphologies of textured Cu surface by nanosecond laser on the inert wetting and reactive wetting, i.e., ethylene glycol/copper and tin/copper wetting systems, was studied by using modified sessile drop methods. To create different surface roughness, the microcosmic morphologies with different spacing of grooves were constructed by nanosecond laser. The results showed that the inert wetting (ethylene glycol/copper) was consistent with Wenzel model, while the reactive wetting results deviated from the model. In Sn/Cu reactive wetting system, the interfacial evolution in the early stage and the pinning of triple line by the precipitated $\eta\text{-Cu}_6\text{Sn}_5$ caused the rougher surface and the worse final wettability. When the scale of artificial roughness exceeded the roughness that was caused by interfacial reaction after reaching the quasi-equilibrium state at interface, the final wettability could be improved.

1. Introduction

The roughness of the surface could be a factor which influences the wettability. For the purpose of objective characterization with good reproducibility of results, the smooth surface with very limited roughness is required, usually, in a range of $\sim 2\text{-}10\text{ nm}$, the roughness (R_a) should be dozens of nanometers for the polished metallic surface, and dozens to hundreds of nanometers for the polished polycrystalline ceramic surface. On the other hand, with development of soldering and brazing technology, a sound joint is not just depended on the reaction at interface, and some uncertain failure may also be caused due to the brittleness of reaction products. The factitious microcosmic topography of surface may be a method to control wettability, and then the dependence of interfacial reaction could be alleviated.

Although the effect of roughness or surface topography

on the wettability has been developed by Wenzel model since 1936^[1], some controversies are still remained in a reactive wetting system, especially for the reactive wetting at high temperatures. As described by Wenzel model, the apparent contact angle can be predicted as

$$\cos\theta_a = w_r \cos\theta_y \quad (1)$$

where θ_a and θ_y are the apparent contact angle on the rough surface and the contact angle on the smooth ideal surface, and w_r is the area ratio of rough surface to smooth surface. Theoretically, when θ_y is below 90° , the increased roughness would improve wettability, and vice versa. However, in the reality, the apparent contact angles are more or less deviated from the predicted value of Wenzel model. Palasantzas et al.^[2] indicated that the critical transition angle was not 90° , and should be smaller than 90° , and further decreases with increasing a roughness exponent H . Wu et al.^[3] suggested that the wettability of

*Corresponding Author:

Qiaoli Lin,

State Key Laboratory of Advanced Processing and Recycling of Non-ferrous Metal, Lanzhou University of Technology, Lanzhou, 730050, China;

Email: lqllinqiaoli@163.com

the compound forming reactive wetting system would be worsening by a rough surface of substrate. Chen et al. [4] developed a theoretical model and verified the wetting behavior experimentally. However, the conflict with Wu's viewpoint [3] was raised, as predicted by Chen et al. [4], the wettability in a reactive system could be promoted with less active addition. Also, Satyanarayan and Prabhu [5] found that the rough surface can improve wettability in the wetting of SAC solders/Cu system, which is a typical reactive wetting system. In the study of Al/h-BN reactive wetting system, Shen et al. [6] considered the different roughness of h-BN surface was the key factor which caused the reported contact angles were so scattered, and also showed the smoother surface and the smaller contact angle, i.e., the wettability would be worsen by the increased surface roughness. Further, Chen and Duh [7] also showed the wettability of solders would be degraded as the substrates become rough in the wetting of Sn-Bi/Cu system. After investigating about the wetting of sixteen materials combinations at room temperature and high temperatures with the selection of atomic liquid (metallic liquid) and molecular liquid (organic liquid), Hitchcock et al. [8] suggested wettability would be deteriorated by roughening a substrate whether of wetting ($\theta_Y < 90^\circ$) and non-wetting ($\theta_Y > 90^\circ$) system. In the study of the reactive wetting of Cu-Sn-Ti and Ag-Cu-Ti alloys on SiC, Tillmann et al. [9] showed no distinct correlation between roughness and wettability. Kramer et al. [10] tried to use Cassie-Baxter model explained the effect of microtextured surface topography on the wetting of In and Sn film by liquid Ga-In alloys, but found that the results only showed a good agreement prior to reactive wetting. In the reactive wetting of CuAgTi/alumina system, the results were obtained by Voytovych et al. [11], indicated that the wetting did not vary significantly with the roughness of the solid. To sum up, whether roughness of the surface would promote or deteriorate wettability in a reactive wetting system at high temperature is still ambiguous, as well as the factor caused divergence.

In this work, the polished Cu surface was textured by nanosecond laser. The liquids, ethylene glycol and pure Sn, were selected, which has the similar contact angles on Cu surface, and also the comparison between molecular and atomic liquids were considered. The textured Cu surface with different roughness was studied. The purpose of this work is to reveal the key factors on the wettability.

2. Experimental Procedure

The substrates of Cu were in a purity of >99.99% and dimension of 20 mm×20 mm×5 mm. Ethylene glycol and Sn with a purity of >99.9% and >99.999% were selected.

The surface of Cu substrate was firstly polished to the roughness (R_a , the mean deviation in contour arithmetic) of ~ 30-50 nm in a tested distance of 2 mm, and then, some substrates were selected for surface laser texturing. The substrates were degreased with acetone and dried by blowing dry air, and then textured by HY-TS20A fiber nanosecond laser machining. The textured morphology was further characterized by infinite focus optical 3D surface metrology (Infinite Focus G4, Alicona Imaging GmbH, Austria).

For the wetting of ethylene glycol/Cu, the experiments were performed by optical surface analyzer (OSA60, NBSI, China); For the wetting of Sn/Cu, because of oxygen partial pressure of atmosphere, the wetting experiments were performed under a high vacuum ($\sim 3-4 \times 10^{-4}$ Pa) by designed device, as described in detail elsewhere [12]. The improved sessile drop method was adopted for the study of Sn/Cu. The advantage of this method, especially for a metallic system, the effect of original oxide film can be alleviated, i.e., the substrate was annealed at high temperature under a high vacuum before wetting. In the vacuum chamber, the substrate was placed on the holder horizontally, and metallic block was stored in a stainless-steel tube outside heating zone. The chamber was vacuumed to a high vacuum ($\sim 5-7 \times 10^{-4}$ Pa), and then the substrate was heated to 700 °C at a rate of 20 °C/min, and dwelling for 10 min, finally cooled to the experimental temperatures. After such a treatment, the covered oxide film on substrate can be broken, and the wetting behavior would be close to the intrinsic behavior. As the experimental temperature was stable, the drop was transferred to the surface of substrate. Meanwhile the camera recorded the variation of the whole wetting process.

After wetting experiments, the profiles of drop were analyzed by Surface Meter Elements analysis software (developed by BNSI company, China) to calculate the contact angle and drop base radius. Selected wetting couples were sectioned and polished for microstructural observation using a scanning electron microscope (SEM, FEG 450, Netherlands) equipped with energy dispersive spectrometers (EDSs) in a spot size of ~2 mm and an optical microscope (OM, MEF-3, Austria) for analysis.

3. Results and Discussion

The square texture with different spaces was constructed by nanosecond laser. The spaces are 50 mm, 75 mm, 85 mm and 100 mm. The typical textured surface of space ~ 85 mm as well as the three-dimensional morphology were shown in Figures 1 (a) and (b). Because of the texturing process by spot laser, the structure was

similar with tight stamp hole. The depth, after laser ablation, is in $\sim 1\text{--}2\text{ mm}$, which is much smaller than Chen's work^[4], but the spaces between two stripes are wider. By varying the space, the different roughness can be obtained, as shown in Figure 1(c). The linear variation of space with roughness indicates the regular controlled morphologies can be obtained by nanosecond lasers.

In the inert wetting system, i.e., the wetting of ethylene glycol/Cu system, the contact angles of ethylene glycol on polished Cu surface are almost invariant, are $\sim 34.1^\circ$, as shown in Figure 2(a). With increase of roughness (or decrease of line spacing by ablation), the pinning of triple line moving is obvious. The decrease of contact angles becomes slow also monotonous, which always take several seconds until reached final contact angle. Based on the obtained actual morphology, the area rate in Equation (1), w_r , can be calculated. The final contact angle vs. w_r has a good linear relationship, as shown in Figure 2(b). The intercept, when $w_r=1$, the intrinsic contact angle for ethylene glycol on ideal smooth Cu surface can be deduced is $\sim 36^\circ$. Also, the limitation of w_r can be calculated for perfect wetting, is ~ 1.33 . When w_r is larger than that value, the wetting type may change from Wenzel model to Cassie model (heterogeneous wetting with air).

The results of the wetting of ethylene glycol/Cu show a good agreement with Wenzel model, i.e., the wettability can be improved definitely with the increase of roughness.

For the reactive wetting, Sn/Cu system, so many complex factors would cause the scattered data. The oxide film of the substrate and interfacial reaction are the main factors. As shown in Figure 3(a), the wetting behavior was influenced by the initial conditions, significantly. Without pre-heat treatment before dropping, the droplet was transferred when temperature was stable at 250°C , the non-wetting of initial contact angle ($\sim 112^\circ$) can be received as well as the slow spreading velocity. As the substrate was first heated to 450°C at a rate of $20^\circ\text{C}/\text{min}$ and isothermal dwelling for 10 min, and then cooled to 250°C , the initial contact angle was decreased to $\sim 68^\circ$, and also the spreading was accelerated. After anneal at 700°C for 10 min, the effect of oxide film on the substrate can be relieved. The final contact angles almost do not depend on the anneal process, are $\sim 34^\circ$, which may due to the high reactivity between Cu and Sn. The effect of surface texturing morphology, as shown in Figure 3(b), the textured morphology would cause a poor wettability, i.e., the larger initial and final contact angles comparing to polished one, also the spreading was slowing down.

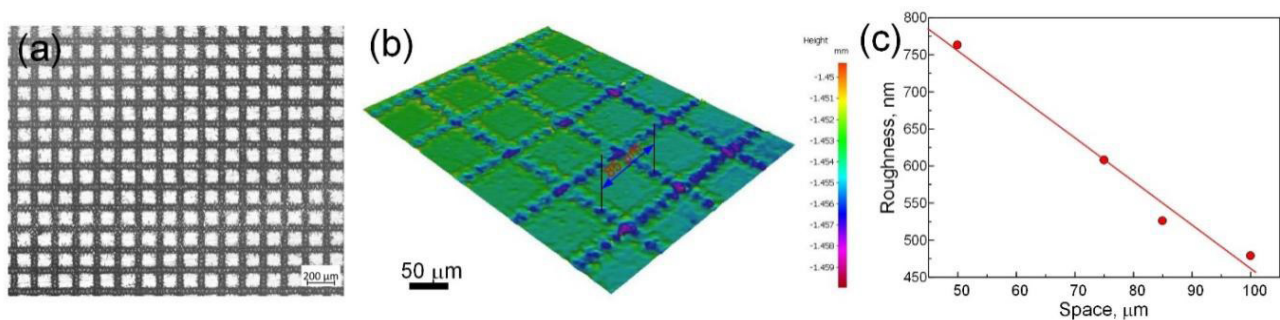


Figure 1. Images of Cu substrate surface by nanosecond laser textured (a) 2D profile and (b) 3D profile; (c) Roughness as a function of space for nanosecond laser textured.

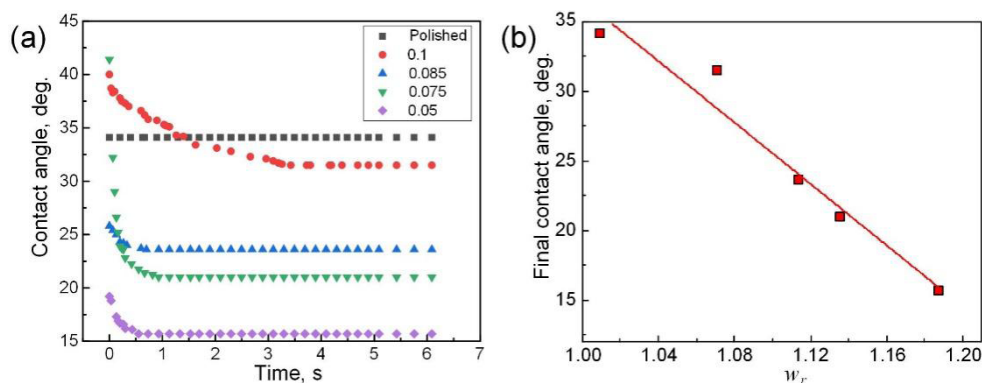


Figure 2. (a) Variations with time of the contact angle of ethylene glycol spreading on textured Cu substrate with different space at room temperature; (b) Final contact angle as a function of w_r for ethylene glycol/textured Cu system.

Obviously, the abnormal phenomenon is inconsistent with Wenzel model, as shown in Figure 3(c). The rougher the surface caused the poor wettability in the Sn/Cu reactive wetting system.

The cross-sectional microstructures of the interface were shown in Figure 4. The typical continuous bilayer structures can be observed. Based on the EDS results, Cu_3Sn layer is the layer contacted with Cu, and Cu_6Sn_5 layer is the layer contacted with liquid. The textured morphology cannot be distinguished in all structures. As be mentioned above, the textured micro-groove in a depth only $\sim 1\text{--}2\text{ }\mu\text{m}$, which can be easily covered up during reaction.

The deviation from Wenzel model should also be related to the interfacial reaction. Chen et al.^[4] proposed a model, for the “non-composite surface” case (Sn-based solder/Cu case), the variation of total energy can be expressed as the increased area of interface multiply the interfacial tension. However, the model is suitable only for inert system. As a reactive wetting system, the interfacial area is varying during reaction as well as interfacial tension. The first stage of the reaction at interface is the dissolution, i.e., the dissolution of Cu into liquid. The laser textured micro-grooves would become flat by dissolution due to the sharp-angled effect, meanwhile, the precipitation of reaction product (IMCs) would further cause the interface become flat. The critical nucleation radius r^* of the precipitation of $\eta\text{-Cu}_6\text{Sn}_5$ or $\varepsilon\text{-Cu}_3\text{Sn}$ can

be expressed as,

$$r^* = 2\sigma_{\eta(\varepsilon)L}T_e/L_e\Delta T \quad (1)$$

where T_e is the equilibrium precipitation temperature, 680 K for η phase and 871 K for ε phase^[13], L_e is the fusion heat per unit volume ($8.69 \times 10^8\text{ J/m}^3$ for η phase and $8.01 \times 10^8\text{ J/m}^3$ for ε phase^[13]), ΔT is the undercooling of η or ε phase and $\sigma_{\eta(\varepsilon)L}$ is the interface energy between precipitated phase and liquid solder (0.09214 J/m^2 for $\sigma_{\eta L}$ and 0.1659 J/m^2 for $\sigma_{\varepsilon L}$ ^[14]). r^* can be calculated, is $\sim 0.9\text{--}1\text{ nm}$ which is much smaller than the scale of laser textured roughness. On the other hand, for a heterogeneous nucleation, the micro-groove (concave interface) would decrease the Gibbs free energy for nucleation, and then increase the nucleation rate. Therefore, the micro-groove would be filled IMCs due to the preferred nucleation, and then made the interface become flat. This stage took place only in milliseconds^[15]. Therefore, in the early stage, the interface with the smaller roughness is much easier to be smooth. The smoother surface and the lower thermodynamic barrier for nucleation for the initial stage, which induced better initial wettability.

However, the roughness caused by the precipitated phase may further cover up the original laser textured morphology. When the size or thickness of grown precipitated phase was over the scale of original roughness, the wettability might be determined by the roughness of precipitated phase ($\eta\text{-Cu}_6\text{Sn}_5$,

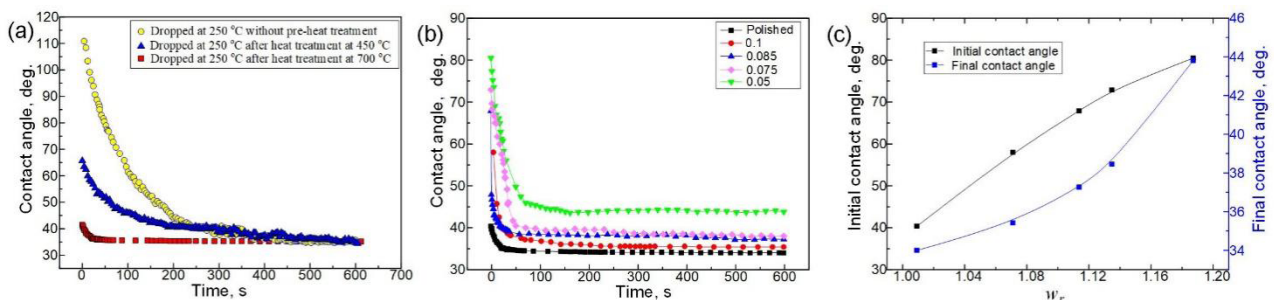


Figure 3. Variations with time of the contact angle of Sn droplet spreading on Cu substrate (a) with different pre-heat treatment temperature and (b) with different space at 250 °C; (c) Initial contact angle and final contact angle as a function of w_r for Sn/textured Cu system.

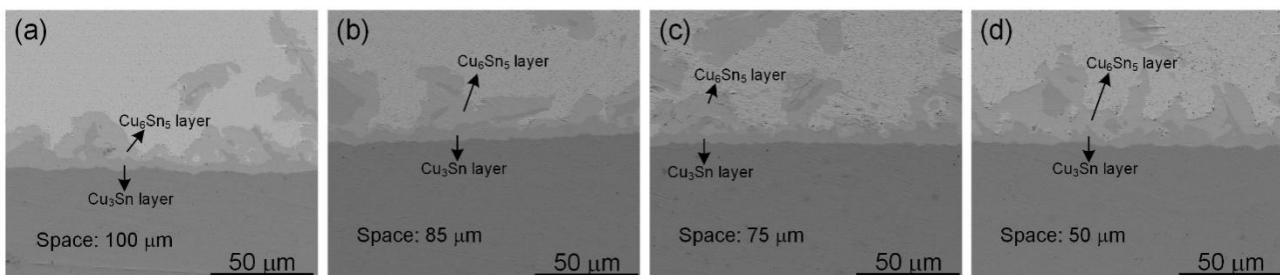


Figure 4. Cross section micro topography of wetting Sn drop on Cu substrate with difference space: (a) 100 mm; (b) 85 mm; (c) 75 mm; (d) 50mm.

phase). The growth kinetics of Sn-Cu IMCs can be described by, $D \approx t^n$, where D is the thickness of η -Cu₆Sn₅ layer, and $n \sim 1/3$ which is related to grain boundary diffusion and limited by the coarsening of the microstructure and elimination of fast mass diffusion paths^[16]. In 100s (the wetting is almost in equilibrium), the thickness of η -Cu₆Sn₅ layer is ~ 4.6 μ m, which is larger than the depth after laser ablation. And then, the roughness was determined by the precipitated η -Cu₆Sn₅ phase. Therefore, the final wettability was weak dependent on the original roughness in this study. When the scale of artificial roughness exceeded the roughness that was caused by interfacial reaction after reaching the quasi-equilibrium state at interface, the final wettability may be improved by texturing process before wetting.

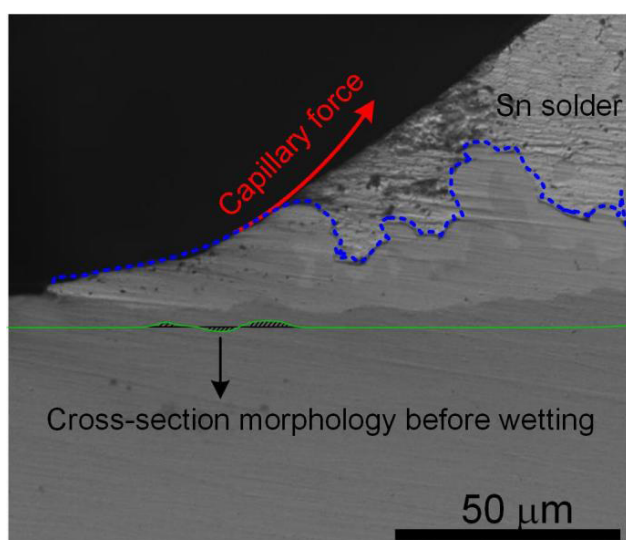


Figure 5. Cross section of the triple line region of Sn/Cu wetting system

On the other hand, the rougher surface would cause the higher probability for the pinning of triple line. The typical configuration at the position close to triple line was shown in Figure 5. The triple line was stopped at the edge of η -Cu₆Sn₅ layer. The shaded area of the green solid line in Figure 5 is the cross-sectional morphology after laser textured. As can be seen, although the original laser textured morphology would be covered up by the nucleation of IMC in the early stage (as mentioned above), the significant mass transfer reaction at that position under the capillary force would prompt the growth of IMCs to the perpendicular direction, and then form a barrier that prevents the triple line from moving. Finally, the triple line was pinned by η -Cu₆Sn₅ layer. Therefore, the rougher surface and the worse final wettability can be correlated.

4. Conclusions

In this study, Wenzel model was verified by the wetting

of laser textured Cu surface by ethylene glycol and tin, as the inert and reactive wetting systems. The obtained results indicated that the inert wetting system had a good agreement with Wenzel model. However, in a reactive wetting system, the rougher surface caused the worse wettability, which is inconsistent with Wenzel model. In the early stage of Sn/Cu system, the fast nucleation process and the small nucleation radius at interface would make the interface smooth. Therefore, the smoother surface and the better initial wettability can be correlated. When the scale of artificial roughness exceeded the roughness that was caused by interfacial reaction after reaching the quasi-equilibrium state at interface, the final wettability may be improved by texturing process before wetting. The enhanced mass transfer reaction in the laser ablation zone under the capillary force at the triple line would prompt the growth of IMCs to the perpendicular direction, and then pin of triple line. Therefore, the rougher surface and the worse final wettability can be correlated.

Credit Authorship Contribution Statement

Kaibing Xie: Methodology, writing, original draft. Yujie Ge: Data analysis, Editing. Qiaoli Lin: Supervision, Work idea, Revision.

Declaration of Competing Interest

The authors declare that they have no known competing financial interests or personal relationships that could have appeared to influence the work reported in this paper.

Acknowledgement

This work is supported by National Natural Science Foundation of China (Nos. 51665031).

Conflict of Interest

No conflict of interest exists to declare.

References

- [1] R.N. Wenzel, Resistance of solid surfaces to wetting by water, Transactions of the Faraday Society. 28(1936) 988-994.
- [2] G. Palasantzas, J. T. M. D. Hosson, Wetting on rough surfaces, Acta Materialia. 49(2001) 3533-3538.
- [3] M. Wu, L.L. Chang, L. Zhang, X.B. He, X.H. Qu, Effects of roughness on the wettability of high temperature wetting system, Surface and Coatings Technology. 287(2016) 146-152.
- [4] H.Y. Chen, J.K. Peng, L. Fu, X.C. Wang, Solder wet-

- ting behavior enhancement via laser-textured surface microcosmic topography, *Applied Surface Science*. 368(2016) 208-215.
- [5] Satyanarayan, K.N. Prabhu, Spreading behavior and evolution of IMCs during reactive wetting of SAC solders on smooth and rough copper substrates, *Journal of Electronic Materials*. 42(2013) 2696-2707.
- [6] P. Shen, H. Fujii, K. Nogi, Effect of temperature and surface roughness on the wettability of boron nitride by molten Al, *Journal of Materials Science*. 42(2007) 3564-3568.
- [7] Y.Y. Chen, J.G. Duh, B.S. Chiou, The effect of substrate surface roughness on the wettability of Sn-Bi solders, *Journal of Materials Science: Materials in Electronics*. 11(2000) 279-283.
- [8] S.J. Hitchcock, N.T. Carroll, M.G. Nicholas, Some effects of substrate roughness on wettability, *Journal of Materials Science*. 16(1981) 714-732.
- [9] W. Tillmann, J. Pfeiffer, L. Wojarski, Influencing Factors on the Reactive Wetting of Cu-Sn-Ti and Ag-Cu-Ti-Alloys on Silicon Carbide-Microstructural Observations, Effects and Multivariate Modelling, *Advances in Science and Technology*. 88(2014) 172-177.
- [10] R.K. Kramer, J.W. Boley, H.A. Stone, J.C. Weaver, R.J. Wood, Effect of microtextured surface topography on the wetting behavior of eutectic gallium-Indium alloys, *Langmuir*. 30 (2014) 533-539.
- [11] R. Voytovych, F. Robaut, N. Eustathopoulos, The relation between wetting and interfacial chemistry in the CuAgTi/alumina system, *Acta Materialia*. 54(2006) 2205-2214.
- [12] Q.L. Lin, P. Shen, L. Yang, S. Jin, Q. Jiang, Wetting of TiC by molten Al at 1123-1323K, *Acta Materialia*. 59(2011) 1898-1911.
- [13] W. Zhai, W.L. Wang, D.L. Geng, B. Wei, A DSC analysis of thermodynamic properties and solidification characteristics for binary Cu-Sn alloys, *Acta Materialia*. 60(2012) 6518-6527.
- [14] W. Zhai, B. Wei, Direct nucleation and growth of peritectic phase induced by substantial undercooling condition, *Materials Letters*. 108(2013) 145-148.
- [15] R.A. Gagliano, G. Ghosh, Fine, Nucleation kinetics of Cu₆Sn₅ by reaction of molten tin with a copper substrate, *Journal of Electronic Materials*. 31(2002) 1195-1202.
- [16] N. Dariavach, P. Callahan, J. Liang, R. Fournelle, Intermetallic growth kinetics for Sn-Ag, Sn-Cu, and Sn-Ag-Cu lead-free solders on Cu, Ni, and Fe-42Ni substrates, *Journal of Electronic Materials*. 35(2006) 1581-1592.

ARTICLE

Identification of an Appropriate Formulation for Domestic Water Ceramic Filters from Soukamna Clay (Cameroon)

Ngiongbound Nguiamba* Celestine Asobo Yanu Placide Désiré Belibi Belibi

Joseph Marie Sieliechi Martin Benoît Ngassoum

National School of Agro-Industrial Sciences, Department of Applied Chemistry, University of Ngaoundéré, Ngaoundéré, Cameroon

ARTICLE INFO

Article history

Received: 13 July 2021

Accepted: 15 July 2021

Published Online: 20 July 2021

Keywords:

Ceramic filter

Porosity

Permeability

Iron leaching

Soukamna

ABSTRACT

This paper deals with the formulation of ceramic filters having the porosity adapted to domestic potable water treatment. The filters were made from clays and rice husk obtained from the Far North region of Cameroon (Logone Valley). Nine formulations were investigated to choose those that might have the porosity standing between 35 and 50% (the ideal porosity adapted for water treatment). The nine formulations investigated were as follows: clay:rice husk mixture weight ratio 0.7:0.3; 0.8:0.2 and 0.9:0.1 with the particle size of 100:100 microns. The sintering temperatures of 900 °C, 950 °C and 1000 °C were applied for each of the mixtures. The results showed that only filters with weight ratio 0.7:0.3 sintered at 900 °C, 950 °C and 1000 °C had porosity between 35 and 50% with values of 39.41 ± 0.96 ; 40.15 ± 1.59 ; 40.14 ± 1.31 respectively. Mechanical strength, permeability and iron leaching behavior were investigated for these three formulations. The formulation 0.7:0.3 with sintering temperature of 1000 °C had the higher permeability and was the more stable for iron leaching so it is the more adapted for water treatment in terms of flow rate and iron leaching behavior, pore size distribution showed that these filters were macroporous and designed for microfiltration with average pore diameter of 0.46 μm .

1. Introduction

Ceramic filters for water filtration is one of the alternative techniques for treatment of drinking water^[2]. They are made of clay and porogen. Ceramic water filtration is the process of passing water through a porous ceramic material. It is a promising way to reduce the burden of water-borne diseases; it is affordable in terms of cost and made from local resources^[3]. It has been shown that ceramic filters can reduce turbidity^[1] and microorganism from water^[3]. However, any ceramic filter intended to treat domestic water must have a minimal flow rate of 1 L/h^[4]. To get this flow rate the porosity of the filters should be between 35 and 50%^[1], this porosity will

ensure a high flow rate and an efficiency against microbial pollutant^[3]. Previous works have shown that filters based on clays of the Far North region of Cameroon can leach iron on the filtrate. Many parameters could influence the porosity and the leaching behavior of a ceramic filter such as the sintering temperature and the percentage of porogen. Determine the best formulation that ensures the ideal porosity and the lower leaching behavior is therefore a crucial task for a clay-rice husk mixture.

In this research, ceramic filters based on materials from Far North region of Cameroon (clay and rice husk) were formulated. Study of the effect of weight ratio (clay and rice husks) and sintering temperature on porosity of the

*Corresponding Author:

Ngiongbound Nguiamba,

National School of Agro-Industrial Sciences, Department of Applied Chemistry, University of Ngaoundéré, Ngaoundéré, Cameroon

Email: ronnynguiamba@gmail.com

filters was done. This was done to choose the formulation (weight ratio and sintering temperature) that gives the porosity between 35 and 50%. Then the study of the effect of temperature on mechanical strength, permeability and iron leaching behavior of the having porosity between 35 and 50% was done. Finally, pore size distribution was investigated on the formulation with the higher permeability and the lower iron leaching behavior.

2. Experimental

2.1 Sampling of Raw Materials

Clay material was collected at a mining site located at Soukamna (Far North region of Cameroon) altitude 321 m, latitude 10.34716°N and longitude 15.26525°E. Rice husks were collected at Yagoua (Far North region of Cameroon) market. After collected, the clay and rice husks were stored and dried at room temperature in the laboratory. The clay was grind using an artisanal (made of wood) mortar while the rice husk was grind using a grinding mill (farmer mill used to grind corn). The clay and rice husk were sieved through a 100 µm sieve.

2.2 Ceramic Body Preparation

Sieved clay and rice husk were then mixed at different ratios 0.7:0.3, 0.8:0.2 and 0.9:0.1 (by weight) followed by making dough by adding water. This leads to what is called “ceramic paste”. We evaluated the influence of rice husks on the viscosity of Soukamna clay and the influence of time on ceramic paste viscosity.

The ceramic paste was then cast in a cylindrical-shaped mold to make the filter. The resulting ceramic filters were cylindrical in shape, hollow with one side open, and had a height of 5,9 cm and a thickness of 5 mm. The samples were then air dried in the laboratory (temperature of 25 °C) for 2 days after which they were further dried at 105 °C in an electric oven (Crouzet, France) for 24h (to make the samples safer and to remove excess moisture). Afterwards the samples were sintered in a muffle furnace (Nabertherm, Germany) at 3 different temperatures (900, 950 and 1000°C) for 8 hours in 2 steps; firstly, sintering temperature was set up at 500 °C at a rate of 5 °C/min and held for 2 h so that all the pore former would be burned off. Secondly, the sintering temperature was increased up to one of the 3-desired final sintering temperatures (900, 950 and 1000 °C) at a rate of 10 °C/min and held for 2 h. Then the muffle furnace was cooled down gradually to temperature below 100 °C before removing the ceramic filters.

2.3 Ceramic Filters Characterization

Lost in weight of ceramic filters was evaluated by

weighting the ceramic body before and after sintering in order to evaluate the influence of ratio and sintering temperature on ceramic filters lost in weight. The ceramic body (before sintering) was weighted and the weight (M1) was recorded. After sintering the ceramic filters obtained were weighted and the weight (M2) was recorded. Then lost in weight (in percentage) was calculated using the following formula:

$$L = \frac{M1 - M2}{M1} \times 100 \quad (1)$$

The apparent porosity (amount of voids or pores within a volume of porous material) was measured according to the Archimedes method (using water as immersion fluid) [5] as follow: the ceramic filters were weighted and the weight (W1) was recorded. They were then immersed in a beaker of water. Bubbles were observed as the pores in the filters were filled with water. Their soaked weights were measured and recorded. The filters were lightly wiped with a moistened smooth cotton cloth to remove all excess water from the surface, and the saturated weight (W2) was recorded. The porosity was then calculated using the following formula:

$$p = \frac{W2 - W1}{W1} \times 100 \quad (2)$$

Mechanical strength of the filters was measured using the compression method [6]. The filters were clamped with 2 pieces of tests grippers and a stretching force was applied until the filters rupture, the maximum load and elastic modulus were recorded by a dynamometer. The mechanical strength was then obtained by the following formula:

$$MS = \frac{F}{S} \quad (3)$$

Where MS is the mechanical strength (MPa), F is the minimal force that cause the filter rupture and S is the surface area of the filter.

The permeability and leaching tests were done using distilled water as water to filtrate. Each ceramic water filter was filled with distilled water and allowed to filter until they are emptied; this was done for a consecutive 10 h (during 10 days). Each time the filters are emptied, the time required and the volume of filtrate were recorded. The flow rate was then obtained by dividing the volume obtained by the time necessary to empty the filter. The flow rate of a day was the mean of each run for this day. The determination of Iron released in solution was done using a colorimetric method (Molecular absorption spectrometer) with a UV-Visible spectrophotometer (spectroquant Pharo 100 M). The Iron content of the filtrate for a day was the mean of each run for this day. The pore size distribution was determined by mercury intrusion porosimetry. The analysis was performed on a

porosimeter AutoPore IV 9500 V1.

3. Results and Discussion

3.1 Influence of Rice Husks and Time on Ceramic Paste Viscosity

As shown in Figure 1, it can be seen that clay alone (100% clay content in ceramic paste) has the highest viscosity (regardless of time) compared to ceramic paste that contains the rice husks. It is observed a decrease of 58%, 48%, 83%; 60%, 45%, 86% and 67%, 52%, 82% respectively for a clay content of 90%, 80% and 70% respectively for a clay content of 90%, 80% and 70% and for the times 60s, 120s and 180s. This observation suggests that addition of rice husks has the effect of destroying the three-dimensional structure of clay [7] and increasing the interaction forces (Van Der Waals forces in particular) between particles which promote the formation of flocs and aggregates and therefore the decrease of viscosity [8], indeed, it is the three-dimensional structure of clay that is responsible for the viscosity of a clay. However, it is noticed that viscosity for the ratio 80:20 is higher than that of the ratio 90:10; this suggests that when the amount of clay is 80 the amount of silica supplied is such that the water absorption capacity decreases. The ratio 70:30 has the advantage of having a viscosity which does not vary with time and whose value (4 PaS) is closest to those accepted in the ceramic industry (0.2-0.4 PaS) [8].

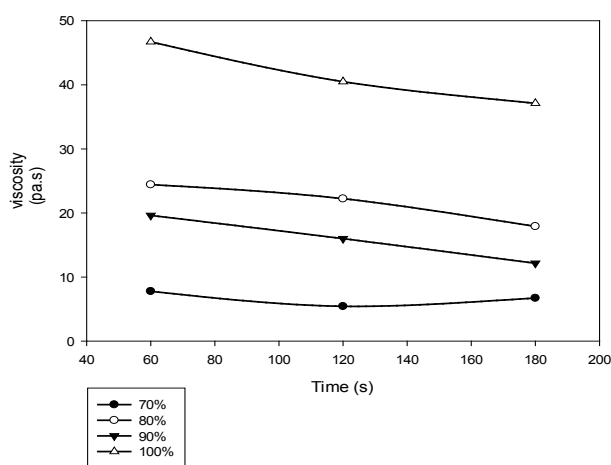


Figure 1. Ceramic paste viscosity

3.2 Ceramic Filters Characteristics

Lost in weight

As shown in Table 1, the temperature did not influence lost in weight of the ceramic filters made with ratio 70:30. This suggests that it is from 30% to above of rice husks content in the paste that rice husks stop to have an effect on clay behavior with sintering temperature. Meanwhile,

with other ratios, it can be seen that lost in weight percentage of ceramic filters raises with temperature. This is due to the development of vitreous phase in these cases [9]. This phenomenon is explained by the fact that raising temperature leads to the move of pores from center towards the surface [10]. Table 1 also shows that lost in weight drops when clay content in the paste raises. This is in accordance with the results of [11] and confirm that rice husks in the paste lead to a compaction of the ceramics.

Table 1. Lost in weight percentage of ceramic filters

% argile	900 °C	950 °C	1000 °C
70	46.09 ± 0.85	45.80 ± 0.67	47.97 ± 0.30
80	36.49 ± 0.08	39.99 ± 0.02	42.44 ± 0.28
90	30.21 ± 1.55	33.16 ± 0.71	35.31 ± 0.12

Apparent porosity

As shown in Table 1, the temperature did not influence the porosity of the filters. However, the percentage of rice husks did. The fact that sintering temperature did not affect the porosity values could be because all the three temperatures studied are on the solid phase of the heat treatment since only liquid phase is the one that is responsible of porosity reduction [11,12]. Meanwhile porosity increases with porogen. This table also showed that only filters of 70:30 at the three sintering temperatures had the target porosity. So, this weight ratio was used for the remaining work.

Table 2. Apparent porosity values of filters in function of sintering temperature and clay content

Clay (%)	900°C	950°C	1000°C
70	39.41 ± 0.96	40.15 ± 1.59	40.14 ± 1.31
80	30.15 ± 0.01	29.34 ± 0.02	28.54 ± 0.34
90	18.65 ± 0.19	21.32 ± 0.08	20.89 ± 1.74

Mechanical strength

Table 2 shows the influence of sintering temperature on the mechanical strength of the filters. It was observed that the mechanical strength remained constant with the increasing of sintering temperature. This result is in harmony with the results of porosity that showed that the porosity of these three formulations was almost the same. In fact, mechanical strength of a ceramic drops when porosity increases [13,14].

Table 3. Mechanical strength of the filters

Clay (%)	900°C (MPa)	950°C (MPa)	1000°C (MPa)
70	0.21 ± 0.03	0.22 ± 0.01	0.23 ± 0.02

Permeability

Figure 2 shows the permeate flux of the ceramic filters.

The result showed that the filters sintered at 1000 °C had the higher permeate flux. This could be because pores diameter and pores density increase with temperature^[15]. So in this case filters sintered at 1000 °C, filters should have higher diameter pores size and the higher permeability.

Iron leaching behavior

Figure 3 and 4 show the evolution of iron content (mg/L) per day and the evolution of cumulative iron content (mg/L) for the filtrate for 10 days trial respectively. Figure 3 shows that the iron content of the filtrate did not exceed 0.3 mg/L which is the maximum tolerable for potable water. Iron leaching is due to the hydroxylation of iron oxides present in the filter matrix when this latter is in aqueous solution^[16]. It was observed that for the first day the higher value (0.133 ± 0.004 mg/L) of Iron content was filtrate of filters sintered at 1000 °C; this is because clay used in this work is non-calcareous clay. In this type of clay amount of iron oxides increases with temperature starting from 700 °C to 1080 °C. Meanwhile

it was observed that iron content in the filtrate from filters sintered at 900°C was higher (0.111 ± 0.025 mg/L) than the one from filters sintered at 950 °C (0.088 ± 0.012 mg/L). This could be because at 950 °C the Iron is in form of Hematite (Fe_2O_3) that is more stable than magnetite (Fe_3O_4) present at 900 °C^[16]. From Figure 4 it was observed that filters sintered at 900 °C were the less stable with the higher cumulative iron content. The cumulative data for sintering temperature of 1000°C and 950°C are around the same. This meaning that the level of iron crystallization is almost the same for these two temperatures^[17].

Due to the higher permeability lowest cumulative iron content on the filtrate, the sintering temperature of 1000 °C was definitely chosen like the adequate temperature for producing ceramic filters. Pore diameter distribution was then investigated for filters sintered at 1000 °C.

Pore diameter distribution

Figure 5 shows the pore size distribution for the ceramic filters. This shows the plot of the derivative of the cumulative curves, dV/d , versus the pore diameter of

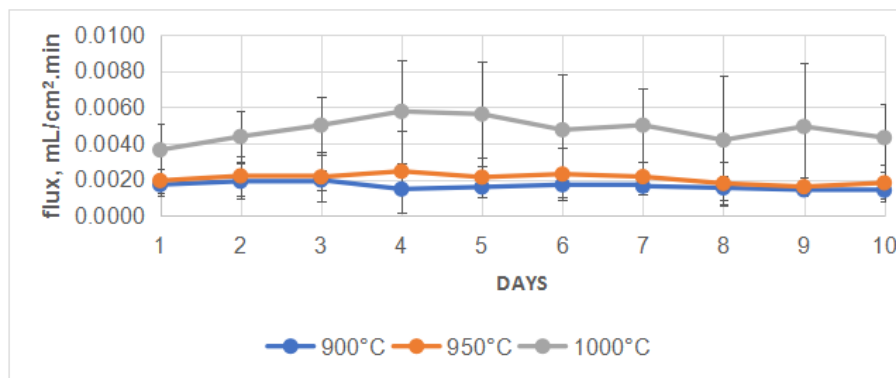


Figure 2. Permeate flux of the ceramics filters

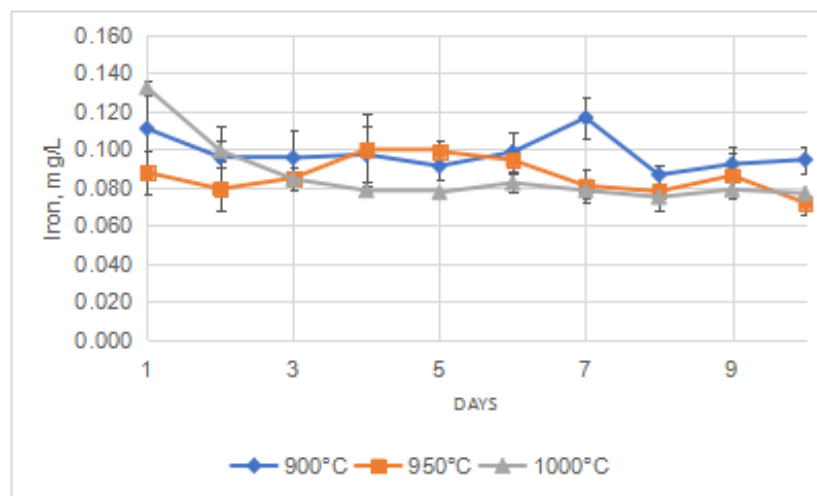


Figure 3. Iron content of the filtrate per day

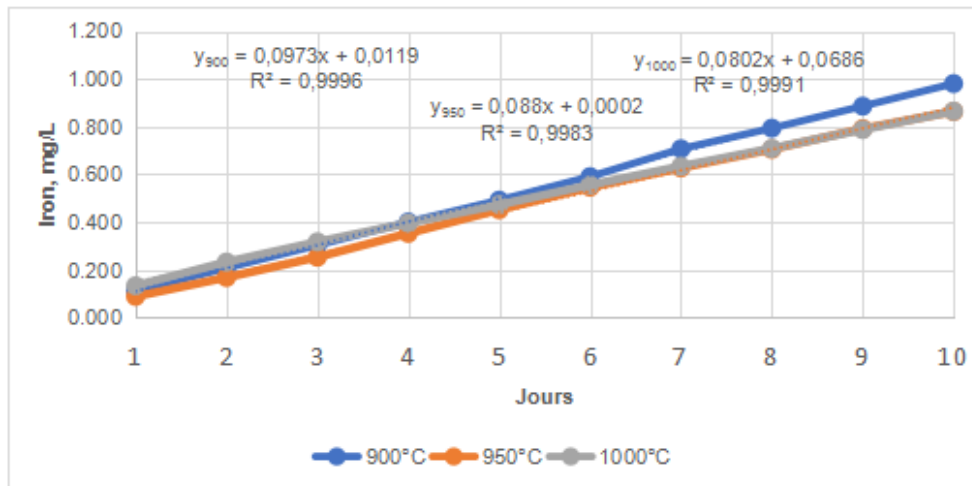


Figure 4. Cumulative Iron content of the filtrate per day

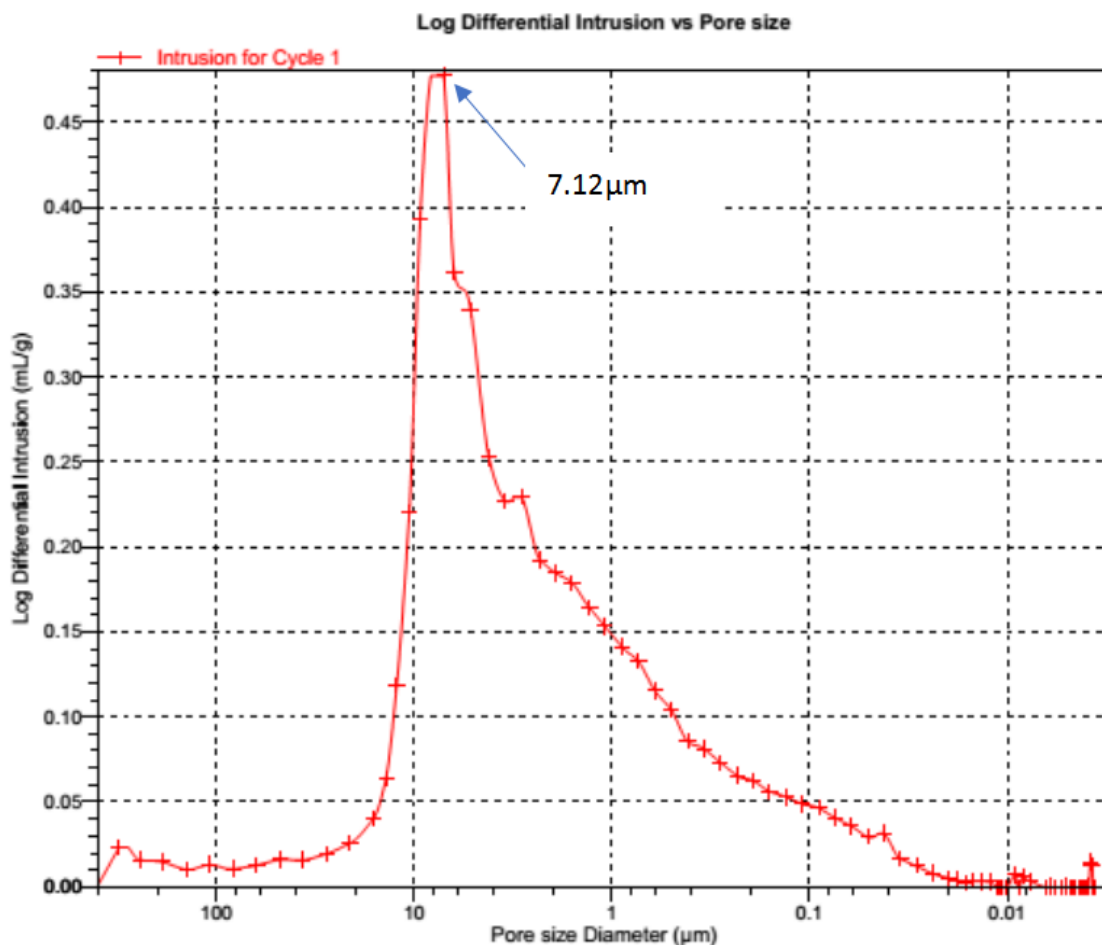


Figure 5. Pore diameter distribution of filters

the studied ceramic filters. The dV/d function is widely used for determination of diameter, which occurs in the penetration of the maximal mercury^[18]. This figure shows that there is a predominant presence of pores with diameters of 0.02 to 21.2 μm , illustrated by the

appearance of a broad peak in this pore diameter range. The summit of this peak (7.12 μm) suggests that pores with this diameter occupy the maximum volume of the filter's matrix. Since average pore diameter is 0.46 μm these filters are macroporous^[19] and designed for

microfiltration.

Table 4. Intrusion data summary

Total Intrusion Volume	0.4168 mL/g
Median Pore Diameter (Volume)	3.8253 μm
Median Pore Diameter (Area)	0.0592 μm
Average Pore Diameter (4V/A)	0.4592 μm
Bulk Density at 0.53 psia	1.3384 g/mL
Apparent (skeletal) Density	3.0270 g/mL
Stem Volume Used	66 %
Porosity	55.7838 %

4. Conclusions

The characterization of ceramic filters showed that to obtain apparent porosity between 35 and 50% the adequate mixture clay:porogen is 70:30 in weight. The results also showed that temperature does not influence porosity because the three temperatures studied are all in the solid phase of heating treatment. Temperature of 1000 °C led to the higher permeability due to the increasing of pore diameter and to the lower iron leaching due to crystallisation of iron with temperature. Pore size distribution on these filters showed that majority of pores has diameter between 0.02 and 21.2 μm and are designed for microfiltration. So that they are able to retain pollutant such as suspended matter that causes turbidity of water. Anyway further research should be done to evaluate the performance of these filters to reduce turbidity.

Acknowledgements

The authors thank

- The International Foundation for Science (IFS),
- The International Fair for Young African Research (IFYAR).

Both for financial support.

References

- [1] Yakub I., Du J., Soboyejo W.O. Mechanical properties, modeling and design of porous clay ceramics [C]. *Material Science and Engineering A*, 558, 21-29.
- [2] Van Halem D., Van Der Laan H., Soppe A.I.A. and Heijman S.G.J. High flow ceramic pot filters [C]. *Water Research*, 124, 398-406.
- [3] Zereffa Enyew Amare and Bekalo Tesfaye Betela. Clay Ceramic Filter for Water Treatment [C]. *Journal of Materials Science and Applied Chemistry*, 34, 69-74. (<https://doi.org/10.1515/msac-2017-0011>).
- [4] Salvinelli C.J. and Elmore A.C. Assessment of the impact of water parameters on the flow rate of ceramic pot filters in a long-term experiment [C]. *Journal Water Science and Technology: Water Supply*, 15, 6, 1425–1432. (<https://doi.org/10.2166/ws.2015.107>).
- [5] Khandan A., Karamian E., Mehdikhani-Nahrkhalaji M., Mirmohammadi H., Farzadi A., Ozada N., Heidarshenas B. and Zamani K. Influence of Spark Plasma Sintering and Baghdadite Powder on Mechanical Properties of Hydroxyapatite [C]. *Procedia Materials Science*, 11, 183-189. (<http://doi.org/10.1016/j.mspro.2015.11.087>).
- [6] Karimizade A., Takallu S. and Mirzaei E. Evaluating the effect of pH on mechanical strength and cell compatibility of nanostructured collagen hydrogel by the plastic compression method [C]. *Nanomedicine*, 5, 3, 180-185.
- [7] Barbato N. Carla, Nele Marcio, Pinto C. José et Silvia C. A. França. Studies of Kaolin Rheology [C]. IX JA-TRAMI, San Juan, Argentina, 2008, 2-11.
- [8] Ayadi Afef Jmal, Soro Julien, Kamoun Amel et Baklouti Samir. Study Of Clay's Mineralogy Effect On Rheological Behavior Of Ceramic Suspensions Using An Experimental Design [C]. *International Journal of Research and Reviews in Applied sciences*, 14, 2, 374-384.
- [9] Zghal H. Baccour, Medhioub M. et Mhiri T. Caractérisation physicochimique et mécanique de matériaux céramiques obtenus à partir des argiles Tunisiennes [C]. *Verres, Céramiques & Composites*, 1, 2, 25-33.
- [10] Nasir Nurulfazielah, Ridhwan Jumaidin, Mohd Zulkefli Selamat, Suhaila Salleh et Kok-Tee Lau. Effect of Different Types of Pore-Forming Agent on the Macro Pore Size of Ceramic [C]. *Applied Mechanics and Materials*, 761, 380-384.
- [11] Al Zubaidy R.Z., Al-Khafaji M.S. and Al-Saadi R.J.M. Compatibility between Hydraulic and Mechanical Properties of Ceramic Water Filters [C]. *Journal of Engineering*, 23, 147-167.
- [12] Dabare L. and Svinka R. Characterization of Porous Ceramic Pellets from Latvian Clays [C]. *Chemija*, 25, 82-88.
- [13] Hettiarachchi P., Motha J.T.S. and Pitawala H.M.T.G.A. Identification of an appropriate body composition for red clay products [C]. *Cerâmica* 56, 339, 285-290.
- [14] Ali Mohammed Sabah, Azmah Hanim Mohamed Ariff, Che Nor Aiza Jaafar, Suraya Mohd Tahir, Norkhairunnisa Mazlan, and Khamirul Amin Maori. Factors Affecting the Porosity and Mechanical Properties of Porous Ceramic Composite Materials [C]. *Materials Science and Materials Engineering*. Oxford: Elsevier; 2017, 1-54. (<http://doi:10.1016/B978-0-12-803581-8.10131-61>).
- [15] Erhuanga Ebele, Isah Bolaji Kashim and Tolulope

- Lawrence Akinbogun. Development of Ceramic Filters for Household Water Treatment in Nigeria [C]. *Art and Design Review*, 2, 6-10. (<http://dx.doi.org/10.4236/adr.2014.21002>).
- [16] Borra Chenna Rao, Mermans Jasper, Blanpain Bart, Pontikes Yiannis, Binnemans Koen and Van Gerven Tom. Selective recovery of rare earths from bauxite residue by combination of sulfation, roasting and leaching [C]. *Journal of Minerals Engineering*, 92, 151-159. (<http://dx.doi.org/10.1016/j.mineng.2016.03.002>).
- [17] Bennour A., Mahmoudi S., Srasra E., Boussen S. and Htira N. Composition, firing behavior and ceramic properties of the Sejnène clays (Northwest Tunisia) [C]. *Applied Clay Science*, 115, 30–38. (<http://dx.doi.org/10.1016/j.clay.2015.07.025>).
- [18] Biron Dionisio da Silva, Bortoluz Jordana, Mara Zeni, Bergmann C. P. and Venina dos Santos. Characterization of Mullite Ceramic Membranes and their Application in the Removal Escherichia Coli [C]. *Materials Research*, 19, 513-519. (<http://dx.doi.org/10.1590/1980-5373-MR-2015-0301>).
- [19] Sotomayor J. Francisco, Katie A. Cychoz and Matthias Thommes. Characterization of Micro/Mesoporous Materials by Physisorption: Concepts and Case Studies [C]. *Accounts of Materials & Surface Research*, 3, 34-50.

ARTICLE

A Constitutive Modeling and Experimental Effect of Shock Wave on the Microstructural Sub-strengthening of Granular Copper

A. D. Sharma^{1*} A. K. Sharma² N. Thakur³

1. Department of Physics, Government College Chowari, Chamba, 176302, India

2. Om Sterling Global University- Hisar, Haryana, 125001, India

3. Department of Physics, Himachal Pradesh University, Shimla, 171005, India

ARTICLE INFO

Article history

Received: 25 August 2021

Accepted: 27 August 2021

Published Online: 30 August 2021

Keywords:

Shock waves

Wide angle x-ray diffraction

Microstructure

FE-SEM

Laser diffraction

Microhardness

ABSTRACT

Micro-sized copper powder (99.95%; $O \leq 0.3$) has been shock-processed with explosives of high detonation velocities of the order of 7.5 km/s to observe the structural and microstructural sub-strengthening. Axisymmetric shock-consolidation technique has been used to obtain conglomerates of granular Cu. The technique involves the cylindrical compaction system wherein the explosive-charge is in direct proximity with the powder whereas the other uses indirect shock pressure with die-plunger geometry. Numeric simulations have been performed on with Eulerian code dynamics. The simulated results show a good agreement with the experimental observation of detonation parameters like detonation velocity, pressure, particle velocity and shock pressure in the reactive media. A pin contactor method has been utilized to calculate the detonation pressure experimentally. Wide angled x-ray diffraction studies reveal that the crystalline structure (FCC) of the shocked specimen matches with the un-shocked specimen. Field emissive scanning electron microscopic examination of the compacted specimens show a good sub-structural strengthening and complement the theoretical considerations. Laser diffraction based particle size analyzer also points towards the reduced particle size of the shock-processed specimen under high detonation velocities. Micro-hardness tests conducted under variable loads of 0.1 kg, 0.05 kg and 0.025 kg force with diamond indenter optical micrographs indicate a high order of micro-hardness of the order of 159 H_v. Nitrogen pycnometry used for the density measurement of the compacts shows that a compacted density of the order of 99.3% theoretical mean density has been achieved.

1. Introduction

In the prevailing atmosphere of worldwide militarization and an age of nuclear engineering, the use of light sustainable metals is increasing due to their high ductility, malleability and high temperature or corrosion resistant properties. An excellent thermal and electrical conductivity with intrinsic strength of formability, ductility and corrosion/fatigue

resistance make non-magnetic copper components a premier choice in the aerospace industries^[1-5]. The solidification of commercially available or chemically/physically synthesized Cu powder involves hydraulic or isostatic processing, metal injection molding or sintering. Distinctive challenges arising on the solidification/ compaction of powders are due to deterioration of fine grained structure as well as formation

*Corresponding Author:

A. D. Sharma,

Department of Physics, Government College Chowari, Chamba, 176302, India;

Email: ads.hpu@gmail.com

of undesired phases in the crystal structure that may result into weak sub-structural strengthening and poor mechanical properties. These powder metallurgical processes due to the high capital investment and extended operating period do not provide satisfactory microstructural sub-strengthening [6-9].

Rapid solidification by explosives is gaining a particular importance in the field of materials science and powder metallurgy wherein the destructive force is channelized for constructive roles. Explosives have number of novel applications in agriculture, forestry, civil engineering, drilling, cutting, welding, cladding and forming of metals, powder metallurgy and manufacturing industries in high temperature and pressure regime. The explosively generated shock wave compaction is quite advantageous due to its controlled detonation pressure that directly transmits shock waves to the powdered materials. Compaction of materials by shock waves utilizes the extremely rapid and intense deposition of energy at the particle surfaces; causes shape deformation and thereby produce inter-particle bonding and keep the compacts homogeneous throughout as well. The high pressure pulse acts only for microsecond offers no opportunity for the grain-growth or formation of undesired phases. The high pressure is accompanied by high temperature which melts the particle surface and is responsible for solid state diffusional bonding of the particles whereas the high cooling rates of the order of $\sim 10^5$ K/s does not allow the material to melt [10,11]. Therefore, this type of rapid solidification retains the original crystalline and microstructure of the compacts. The basic problem while working with explosive compaction of metals and alloys is the controlled detonation pressure. To avoid rigorous repetition of field trials for optimization of shock wave parameters, a well coupled Computer simulations by using ANSYS software AUTO DYNE-2D in Eulerian mesh has been performed before carrying out the actual experiments.

This paper presents the computer simulation studies and experimental verification of shock consolidated granular copper powder. The crystal structure and the corresponding microstructure before and after shock compaction has been studied and correlated with the theoretical aspects of shock consolidation phenomena. The computational results are in upright agreement with the experimental outcome.

2. Experimental

The experimental method involves a cylindrical compaction system in which powder container ampule is surrounded by a Perspex pipe and the space in-between is tapped gently with high energetic explosive. The ampule

is made of mild steel to withstand with shape deformation with a conical top and plane bottom plugs. The plugs are fabricated with annular grooves so that during rapid solidification process the material may flow into those grooves and thus making a single conglomerate [12,13]. An electric detonator is placed on the top center of the explosive loaded assembly which is further connected to a generator capacitor exploder to initiate the detonation reaction. A pin contactor technique is employed to measure the detonation velocity of the explosive in the reactive media. A series of electrical pins is placed through drilled holes on the bottom half of the assembly at various depths which served to determine the arrival time of shock wave as it passes through these electrical pins. The output of these pins is connected to the digital storage oscilloscope where the electrical signal is converted to the voltage pulses by a pulser and the arrival time of shock wave can be determined. Knowing the arrival time and distance between the pins, detonation velocity can be calculated by the following relation:

$$P_{CJ} = \frac{\rho_0 D^2}{\gamma_{CJ} + 1}$$

And the corresponding particle velocity can be calculated by

$$u_p = \frac{D}{\gamma_{CJ} + 1}$$

Where, ρ_0 is density of explosive used and γ_{CJ} is adiabatic exponent of CJ-point with a value of 3 in present case. Upon reaction initiation, a detonation wave on interaction with explosive process a shock wave which traverses down to the explosive column and a rarefaction wave produces a side on pressure thus collectively an axisymmetric shock pressure consolidates the powder material.

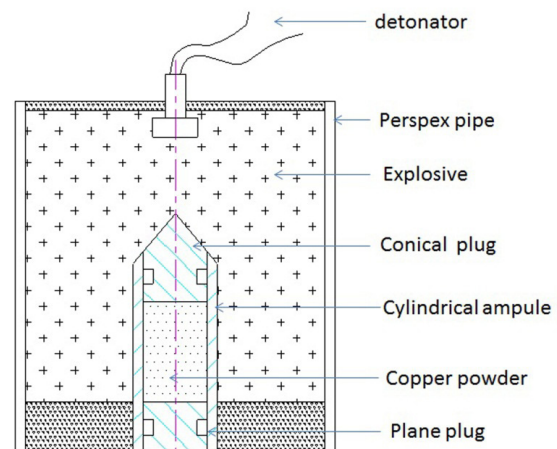


Figure 1. Axisymmetric cylindrical compaction system with explosive in close proximity with Cu.

The recovered specimen is machined for crystal structure, microstructural features and microhardness. Wide angle X-ray Diffraction using X'PERT X-ray detector with step time of 1.0s and step size of 0.02 ($^{\circ}2\theta$) operating at 40KV over the angle range 30 to 80° . The initial powder morphology was examined by using SEM JEOL JSM operating at 25 kV and a pressure of 10^{-5} torr. The microstructural study from the fractured parts of the specimen was observed by FE-SEM at high magnification. The microhardness of the compacted specimen was determined by Lieca microhardness tester with indent load of 50 gf and 100 gf loads. The particle sizes were measured by using small angle laser light scattering method whereas the density of the final product was measured by using nitrogen pycnometry.

The shock parameters have been computed by non-linear transient numeric simulation using an Eulerian code in AUTODYN 2D workbench. The equation of state for the powder and distended materials is governed by the Mie-Grüneisen relation:

$$P - P_{ref} = \Gamma \rho (E - E_{ref})$$

$$P_{ref} = \frac{\rho_o c_o^2 \mu (1 + \mu)}{[1 - (s - 1)\mu]^2}$$

$$E_{ref} = \frac{1}{2} \frac{P_{ref}}{\rho_o} \left(\frac{\mu}{1 + \mu} \right)$$

$$\mu = \frac{\rho}{\rho_o} - 1$$

Where, P is the Shock -pressure, ρ_o is initial tapped density, s is fitting parameter obtained by the slope of curve (shock velocity–particle velocity curve) and Γ is Mie Grüneisen parameter with a value of 2 for Cu^[14,15]. The solution is obtained by modeling the consolidation experiment in 2d axisymmetric configuration. The explosive has been modeled by assuming that on detonation, the propagating detonation wave transfers its energy to the surrounding material at the reference density of 1.5 g/cc. The solution of the full set of equations is obtained numerically by using Eulerian space referential. In order to produce infinite boundary conditions, the material flow out and pressure transmission conditions have been applied to the Eulerian space. In order to observe the shock pressure variation with respect to distance from the core, the sensing probes has been placed at the core and also at radial distances of 3mm and 5mm of the powder compact including the compaction ampoule. For the initiation of detonation, the point detonation has been chosen and applied at the top of the set-up as shown in Figure 2.

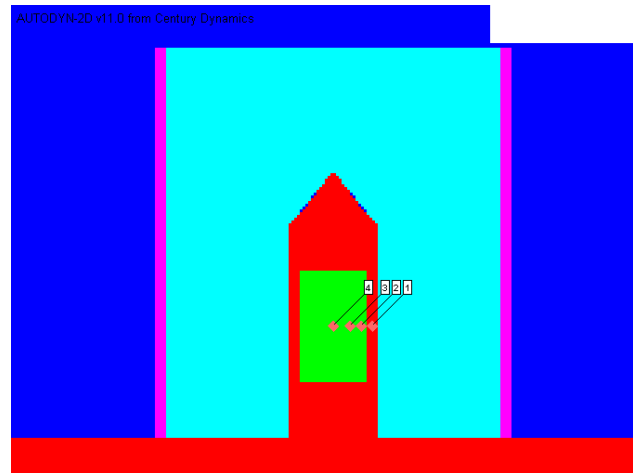


Figure 2. modeling for shock-consolidation set-up with gauge points.

3. Results and Discussion

3.1 Simulated and Experimental Determination of Detonation Velocity

The shock pressures are predicted at the core and also at radial distances of 3 mm and 5 mm of the powder compact including the compaction ampoule. By proper selection of the Eulerian simulation parameters, the modeling of air, copper powder and explosive has been employed to calculate shock pressures with the theoretical values. The granular copper powder, weighing 12.25 g with average particle size of 22 micron, has been filled manually into ampoule by tapping to a density of 4.6 g/cc. The filled ampoule is placed centrally inside the outer tube made of aluminum alloy. A plastic explosive, weighing 0.277 Kg has been filled into the annular space between ampoule and outer tube to a density of 1.5 g/cc.

Figure 3 depicts the simulated detonation pressure profile as the shock wave approaches the gauge points whereas output pulse record obtained by pin contactor method provides arrival time of shock wave as it approaches the electrical pins. The distance at which these pins were inserted into the perspex pipe is known already. Hence, velocity of detonation can be calculated. The experimental average value of detonation velocity is found to be 7.5 km/s which correspond to the detonation pressure of the order of 18.38 GPa. On the other hand simulated detonation pressure is of the order of 17.1 GPa with a net dispersion of 6.9%.

The shock pressures are predicted at the core of the powder compact including the compaction ampoule. The shock pressure at the core has been calculated as 41.3 GPa, wherein $\rho = 8.5$ g/cc, $u_s = 4.744$ km/s and $u_p =$

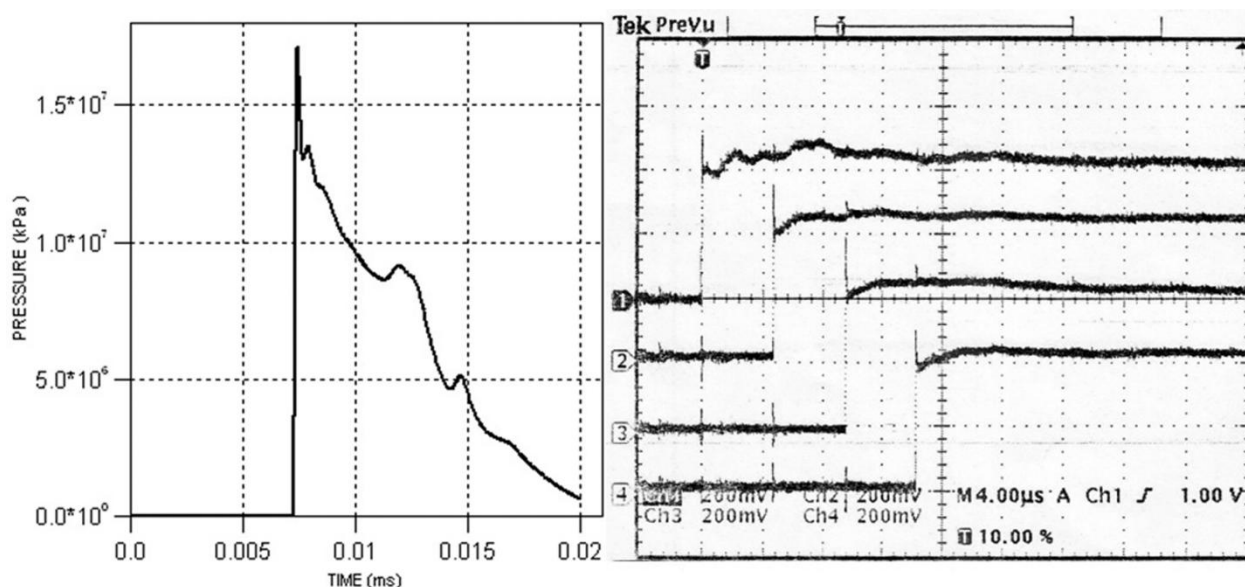


Figure 3. Simulated detonation pressure profile and output pulse record obtained by pin contactor.

1.024 km/s. The simulated shock pressure profile at core is shown in Figure 4, which stipulates a peak pressure of 38.7 GPa. The dispersion between the simulated and theoretically calculated values of peak pressure is 6%.

3.2 Crystal Phase Determination

Figure 5 is wide angle x-ray diffraction (WAXD) pattern of the un-shocked initial and shocked specimen. Peak positions clearly be identified and corresponds to FCC structure for both the specimens. No other peak can be detected in the WAXD pattern is a suggestive of absence of undesired phases in the shocked specimen. This means that the compacts have retained their crystalline structure intact. A little noise in the shocked specimen as compared to the un-shocked specimen can be attributed to the partial amorphization which actually is due to the re-solidified melted regions across the interparticle boundaries and is responsible for the solid-state diffusional bonding between the particles. Another specific feature evident from the WAXD pattern is the peak broadening of the shocked specimen which indicates particle size reduction and complements the theoretical considerations. Under the high pressure of the order of 41.3 GPa the particles undergo plastic deformation mechanism which reduces the particle size^[16].

3.3 Microstructural Analysis

Figure 6 (a) represents initial powder morphology of the granular smooth fine orange-red colored copper particles with fernlike structure. Few small satellite

particles can be seen to attach with large particles with a well-defined dendritic structure. The average particle size as suggested by micrographs is observed to be about 30 μm which matches with the average size taken from the laser diffraction based scattering experiment. A gaussian distribution of the particles corresponds to average mean diameter of 22 μm as shown in Figure 6. The fractured morphology of the consolidated specimen taken from the inner core where the pressure was intense, is shown in Figure 6(b). One feature is quite prevalent that the original dendritic structure of the specimen has remained intact and can be observed without any deformation. The particles are joined together via plastic deformations which is in agreement with the theoretical prediction. The interparticle melted regions get re-solidified under high cooling rates of the order of 10^5 K/s thus maintaining the original microstructure^[17,18]. This behaviour is a clear evidence that micro-structural sub-strengthening has been achieved in this process with specified conditions.

3.4 Microhardness and Density Measurements

The microhardness of the consolidated specimen has been tested with diamond indent loads of 0.1 kg, 0.05 kg and 0.025 kg force. Figure 7 (a) is an optical micrograph of the polished surface of the consolidated copper which appears to have smooth finishing and good uniformity. Figure 7(b) is the optical micrograph with indent loads. It can be discerned from the micrograph that the indent loads have been withheld well by the surface of specimen and no cracking or deformation can be seen. The larger

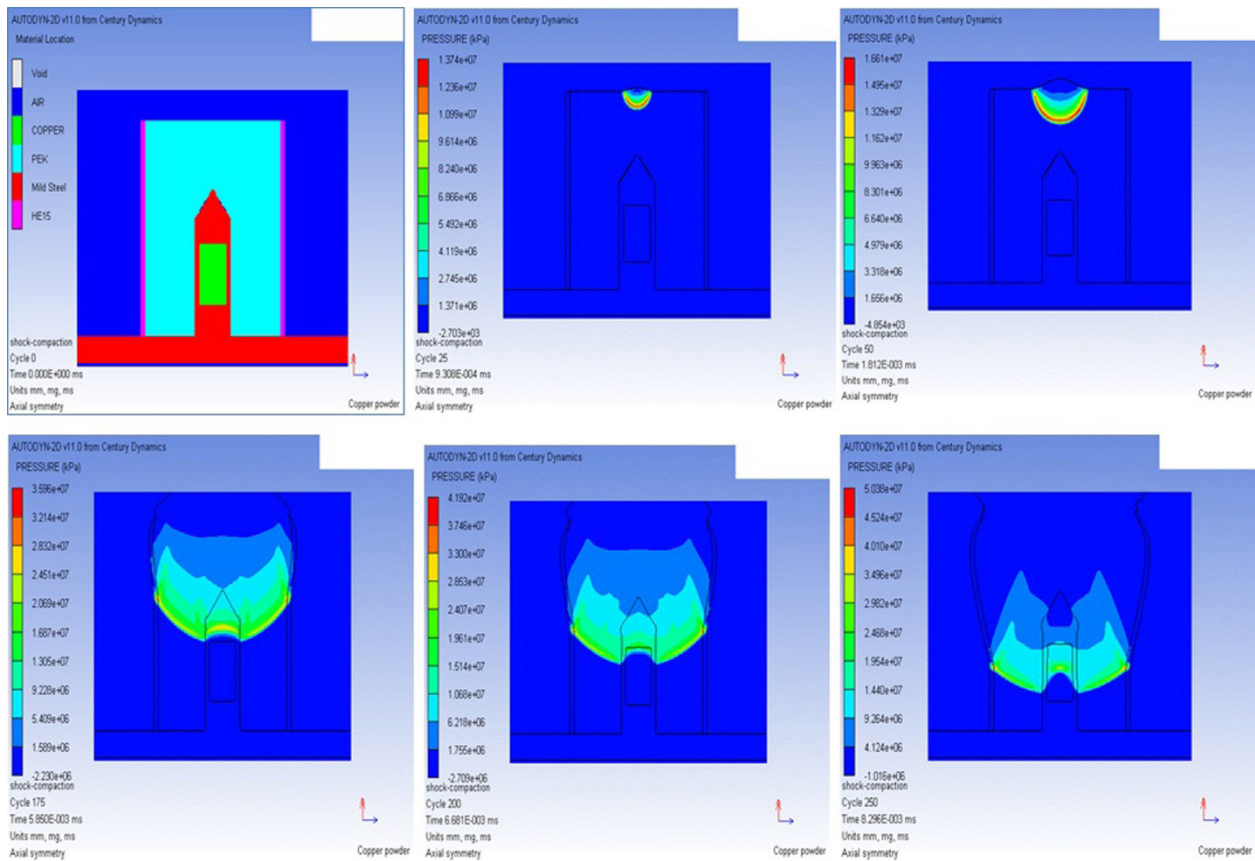


Figure 4. snapshot of the shock wave pressure profile as it traverses down to the explosive consolidation system

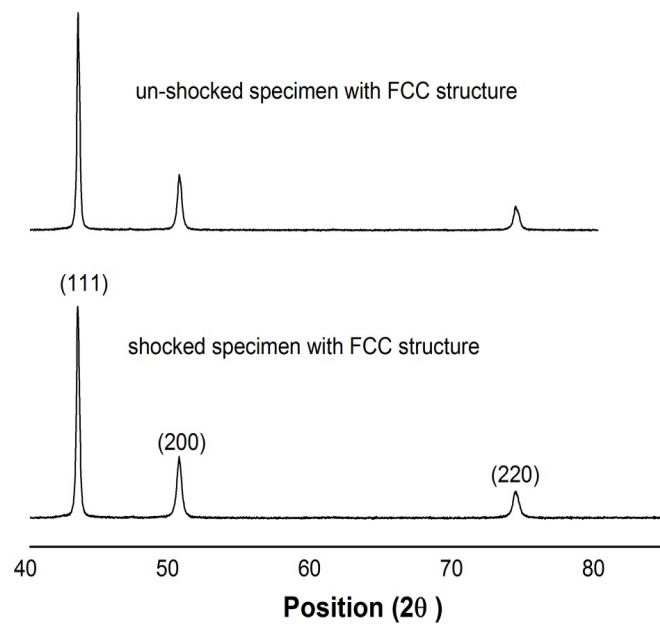


Figure 5. WAXD pattern of un-shocked and shocked granular Cu.

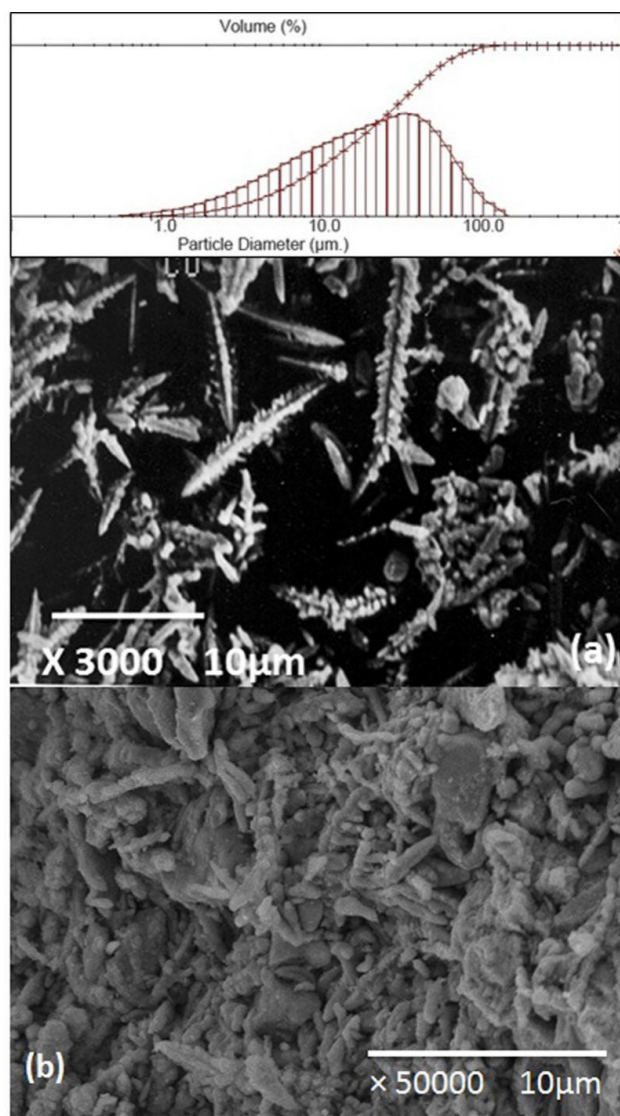


Figure 6. (a) Initial powder morphology showing the dendritic structure; (b) Microstructure from the fractured part of the consolidated specimen showing well bonded structure with intact dendritic structure.

pyramid indent is for 0.1 kg force whereas the smallest is for 0.025 kg force. The density of the final product is measured by nitrogen pycnometry corresponds to a value of 99.3% of the theoretical mean density of Cu.

The observed data with Vicker's microhardness values as per ASTM standard E-92 is shown in Table 1 as follows:

Table 1. Microhardness record obtained under various diamond pyramid indent loads.

Average	Maximum	Minimum	Std. Deviation
154 H _V 0.025	154 H _V 0.025	154 H _V 0.025	0.0
157 H _V 0.05	159 H _V 0.05	155 H _V 0.05	2.19
136 H _V 0.1	136 H _V 0.1	135 H _V 0.1	0.62

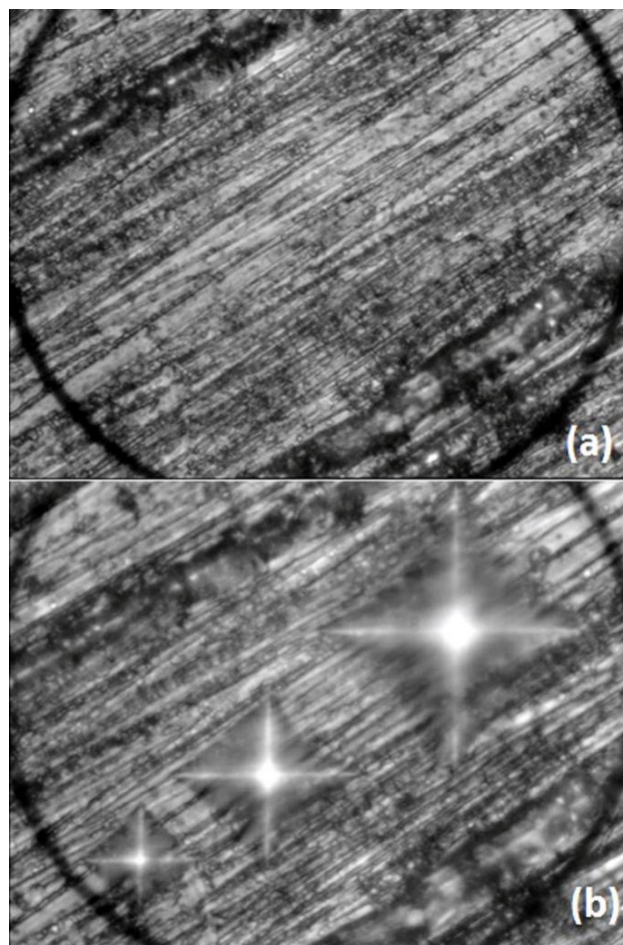


Figure 7. Optical micrographs showing diamond indenters at variable loads.

4. Conclusions

A good sub-structural strengthening for granular Cu has been achieved by using explosively generated shock waves corresponding to a detonation pressure of the order of 18.38 GPa and shock pressure of 41.3 GPa. The computational results obtained by simulations in AUTODYN -2d software in Eulerian mesh proved to be an excellent pre-determination of the shock parameters as the results are in close agreement with the experimental outcome with a dispersion of 6% only. The crystalline structure of the consolidated specimen matches exactly with that of initial specimen without indication of any other phases as revealed by wide angle x-ray diffraction studies. The original dendritic structure remained intact under the shock wave loading without serious melting as conferred by the microstructural studies. An elevated microhardness value of the order of 159 H_V complements the sub-structural strengthening observed by the FE-SEM. Under the controlled conditions of input parameters the specimen can be consolidated close to the theoretical

mean density.

Acknowledgements

The authors desire to acknowledge Defence Research and Development Organization (DRDO), India, for Grant-in-aid Project No. ERIP/ER/0703665/M/01/1044. Special thanks go to the University Grants Commission (UGC-New Delhi), India, for providing Research Fellowship No. F.4-1/2006 (BSR)/11-08/2008. Thanks are also due to USIC facility at H.P. University, Shimla and SAIF/CIL Lab. at Panjab University- Chandigarh and the entire trial team. A distinctive thanks is due to Madan K. Sharma, Yugal K. Yoshi and Rajendra S. Bisht for their necessary assistance and guidance in carrying out the field experiments and numeric simulations.

References

- [1] P.K. Samal, J.W. Newkirk, ASM handbook, Powder metallurgy, 7 (2015).
- [2] J.R. Davis, Copper and copper alloys, ASM International (2001).
- [3] E. Klar, D. F. Berry, Copper powder metallurgy products, ASM handbook, 2 (1990).
- [4] S. Wahyudi, S. Seopryianto, M.Z. Mubarak, Sutarno, IOP Conf. Ser, Mater. Sci. Eng. 395 (2018) 012014.
- [5] P.J. James, Fundamental aspects of the consolidation of powders, Powder Met. Int. 4 (1972) 82.
- [6] L. Avramovic , V. M. Maksimovic, Z Bascarevic, N. Ignjatovic, M. Bugarin, R.Markovic , N.D. Nikolic , Influence of the shape of copper powder particles on the crystal structure and some decisive characteristics of the metal powders, Metals, 9 (2019) 56.
- [7] A.D. Sharma, A.K. Sharma, N. Thakur, Study on the crystal structure and microstructure evolution of shock-processed Titanium powder, J. Met. Mater. Res. 2 (2019) 26-31.
- [8] A.D. Sharma, A.K. Sharma, N. Thakur, Effect of explosive contact and non-contact shock processing on structure, microstructure and mechanical characteristics of aluminium, Appl. Phys. A 111 (2013) 783-789.
- [9] A.D. Sharma, A.K. Sharma, N. Thakur, Shock wave processing of metal powders and their microstructural characterization, AIP Conf. Series: 119 (2011) 1393.
- [10] M.A. Meyers, D. J. Benson, E.A. Olevsky, Shock consolidation: microstructurally-based analysis and computational modeling, Acta. Mater. 28 (1999) 2089-2108.
- [11] C.T. Wei, E. Vitali, F. Jiang, S.E. Du, D.J. Benson, K.S. Vecchio, N.N. Thadhani. M.A. Meyers, Quasi-static and dynamic response of explosively consolidated metal-aluminum powder mixtures, Acta. Mater. 60 (2012) 1418-1432.
- [12] A.D. Sharma, A.K. Sharma, N. Thakur, Crystallographic, microstructural and mechanical characterization of dynamically processed IN718 superalloy, J. Alloys. Comp. 597 (2014) 175-180.
- [13] A.D. Sharma, A.K. Sharma, N. Thakur, Crystallographic and morphological characteristics of explosively compacted copper under various detonation velocities, Phil. Mag. 92 (2012) 2108-2116.
- [14] M.A. Meyers, Dynamic Behavior of Materials, Wiley, 1994.
- [15] M.A. Meyers, D.J. Benson, E. A. Olevsky, Shock consolidation: Microstructurally-based analysis and computational modeling, Acta. Mater. 47 (1999) 2089-2108.
- [16] A.D. Sharma, A.K. Sharma, N. Thakur, Effect of explosive contact and non-contact shock processing on structure, microstructure and mechanical characteristics of aluminium, Appl. Phys. A 111 (2013) 783-789.
- [17] D.G. Morris, Microstructure changes taking place during dynamic compaction of aluminium powders, J. Mater. Sci. 21 (1986) 1111-1117.
- [18] A.D. Sharma, A.K. Sharma, N. Thakur, Crystallographic, microstructural and mechanical characterization of dynamically processed EP741NP superalloy, Metall. Mater. Trans. B 47 (2016) 2479-2486.

ARTICLE

Orange Peel Extract Mediated Silver Nanofluid as Corrosion Inhibitor for X80 Steel in Simulated Oilfield Scale Dissolver

Ekemini Ituen* Chukwudurom Dim Ekerete BoEKOM

Department of Chemistry, Faculty of Science, University of Uyo, Uyo, Nigeria

ARTICLE INFO*Article history*

Received: 25 August 2021

Accepted: 2 September 2021

Published Online: 6 September 2021

Keywords:

Adsorption

Corrosion inhibitor

Orange peels extract

Silver nanoparticles

Electron microscopy

ABSTRACT

Silver nanofluid was prepared by bio-reduction reaction between orange peels extracts (OPE) and silver nitrate and characterized by spectroscopic and microscopic techniques. Colloidal nanoparticles of sizes between 40 – 50 nm and spherical shape were obtained. The nanofluid was applied as anticorrosion additive to inhibit corrosion of X80 steel in simulated oilfield scale dissolver solution (1.0 M HCl) at various temperatures. The nanofluid (OPE-AgNPs) was 98.9 % and 84.3 % efficient at 30 °C and 60 °C respectively as determined by weight loss measurement. In comparison with OPE, OPE-AgNPs shows better corrosion inhibition and higher resistance to thermal degradation. Some kinetic and thermodynamic models were used to characterize the inhibition process. OPE-AgNPs could be optimized and used as alternative anticorrosion additive for scale dissolution liquor in the industry.

1. Introduction

Scales are mineral deposits often accumulated downhole, on topsides or on export terminals during petroleum production. They plug the pipework or permeable reservoir and cause flow problems. They also contaminate the produced fluid. Operators will be forced into relentless and costly effort to keep the pathway clear to maximize production. This is often achieved through descaling or acid wash operations to remove or decommission scales. The solution used for this procedure is often called scale dissolver and is composed mainly of hydrochloric acid of concentration about 1 M^[1,2].

Being acidic in nature, scale dissolvers could create additional problems – corrosive attack on steel materials. Therefore, it is crucial to add corrosion inhibitors to the solution to retard the rate at which the dissolver corrodes the steel surface while maintaining the dissolver in the

desired activity. A wide variety of corrosion inhibitors (ranging from organic to inorganic, to organometallic compounds) are available for this purpose^[3,4]. However, the corrosion inhibitor (CI) needs to be cheap and environmentally friendly, which makes plant extracts to attract tremendous research attention as potential material for use as corrosion inhibitor.

Plant extracts are cheap, readily available and non-toxic. However, plant extracts are easily degraded by heat and biochemical agents. In addition, it is difficult to store extract-based CIs for a long time as it will biodegrade^[3]. Therefore, the need to chemically transform plant extracts into new materials that will not be easily degraded thermally or biochemically, and will exhibit improved inhibition efficiency and longer storage time becomes crucial. In this work, we report the efficiency of a nanofluid obtained by modification of plant biomass extract with silver nanoparticles as a new alternative

**Corresponding Author:*

Ekemini Ituen,

Department of Chemistry, Faculty of Science, University of Uyo, Uyo, Nigeria;

Email: ekeminiituen@uniuyo.edu.ng

corrosion inhibitor for X80 steel in simulated oilfield scale dissolver.

The advantage of nanoscale materials is that they have high size to volume ratio and this makes them more reactive. Nanoparticles prepared from plant extracts have been widely reported. Although the mechanism of formation of the nanoparticles has not been convincingly described, it is generally accepted to occur by bio-reduction reaction. Researchers opine that these nanomaterials have extensive future prospects. Better still, their synthetic process takes a single route and does not require complex tools or high energy. Since there are a wide variety of plants and the biomasses can be obtained in large quantity, it is possible to scale up the production and have a wide range of nanoparticles for various applications. It is on these bases that our interest is channeled to this research direction.

2. Materials and Method

2.1 Extraction

Fresh ripe oranges were acquired from Itam market in Uyo and conveyed to Chemistry laboratory for analyses. The orange biomass was washed for two times in deionized water, peeled, air-dried, milled and weighed (w_0). 10.0 g of the pulverized biomass was extracted in 1.0 L deionized water for 24 h followed, then filtered. The residue was weighed (w_1) after being dried in air. The weight of extract recovered was estimated by determining the difference in weight ($w_0 - w_1$). The extract solution was concentrated to paste form using rotary evaporator, then dried at 45 °C to powder in the oven.

2.2 Preparation and Characterization of Nanofluid

0.5 g/L of the orange peels extract (OPE) was mixed with 1.0 mM AgNO₃ (1:1) at 30 - 50 °C in water bath with constant swirling until colour change was observed. A portion of the colloidal solution was dried to nano-powder in oven at 35 °C while the other portion was stored in amber bottle at laboratory temperature. A small amount of the nano-powder was dissolved in de-ionized water to obtain a colloidal solution of the nanofluid. The nanofluid were analysed for light absorption properties using UV-Vis spectroscopy at 400 – 800 nm. Also, both the extract and nano-powder were characterized by X-ray diffraction (XRD) at $2\theta = 10^\circ - 90^\circ$. Particle size, morphology and shape were also determined by TEM.

2.3 Corrosion Studies

1.0 M HCl was prepared from 37% Analar grade (Sigma

Aldrich) stock and used to simulate scale dissolver. X80 steel coupons of composition: (wt. %) C (0.17), P (0.015), Ti (0.015), Si (0.38), S (0.002), Mn (1.25), Mo (0.20), Nb (0.04), Fe (bal), were used as test specimens in experiments. Specimens were initially immersed in absolute ethanol to remove lubricants, then polished with silicon carbide abrasives various grits until mirror finish was reached. Polished specimens were again cleaned in ethanol, washed in acetone for easy air-drying, then weighed.

Different weights of the nano-powder were measured and used to prepare three different concentrations (0.10 g/L, 0.30 g/L and 0.50 g/L) in 1.0 M HCl. The immersion approach was deployed to carry out weight loss experiments with the X80 steel coupons (dimension = 2 cm x 2 cm) fully suspended in the 1.0 M HCl (blank) and inhibited (containing the nano-powder) solutions at 30, 40, 50 and 60 °C maintained in water bath^[3]. After 24 h of immersion, each coupon was retrieved and cleaned following then ASTM standard procedures (ASTM G1-90)^[5], then reweighed. This was repeated for all test solutions in triplicates and the mean weight loss was determined which was used to compute corrosion rate and inhibition efficiency based on Equation 1 and 2 respectively.

$$C_R = \frac{87.6\Delta m}{\rho A t} \quad (1)$$

$$\%I = 100 \left(\frac{C_{RO} - C_{R1}}{C_{RO}} \right) \quad (2)$$

where the parameters Δm , A , t , ρ , C_{RO} and C_{R1} represent mean weight loss, surface area of coupon (cm²), immersion time (h), density of iron (gcm⁻³), and corrosion rates of blank and inhibited solutions, respectively.

3. Results and Discussion

3.1 Formation and Characteristics of the Nanomaterial

The nanoparticles were formed within 45 minutes as signalled by changing colour to dark brown. When allowed to stand for another 48 h, the dark brown colour remained unchanged signifying that bio-reduction reaction had completed. Also, a homogeneous nanofluid without sediment was obtained which indicates that the nano-powder is soluble in water. Comparing the UV-Vis spectra of the extract solution and the nano-fluid, it was observed that there was difference in their plasmon absorption (Figure 1). While the extract absorbed at $\lambda_{\max} = 545$ nm, the nanofluid absorbed at $\lambda_{\max} = 496$ nm. The wavelength, $\lambda_{\max} = 496$ nm, falls within previously reported Plasmon

absorption range of 400 - 500 nm^[6] for plant biomass mediated silver nanoparticles (AgNPs), supporting that orange peels extract- silver nanoparticles (OPE-AgNPs) were completely developed. Absorption in the UV-Vis region often leads to electronic transitions. Depending on the identities of the phyto-compound, transitions such as $\sigma \rightarrow \sigma^*$ could occur in single bonded molecules, $n \rightarrow \pi^*$ in molecules containing lone pair of electrons and $\pi \rightarrow \pi^*$ in double bonded, triple bonded and molecules with conjugation.

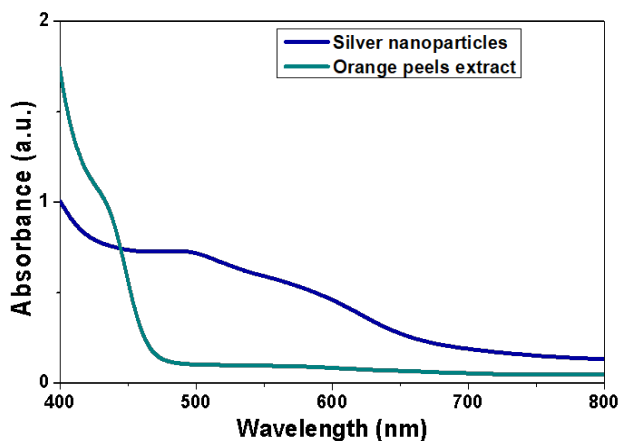


Figure 1. UV-Visible spectrum of orange peels extract and the silver nanofluid

To further investigate the nature of the nano-powder, XRD diffraction patterns of the pure extract and the OPE-AgNPs were obtained (Figure 2). No well-resolved peaks were observed with the spectrum of OPE whereas distinct well-resolved peaks were observed for OPE-AgNPs at $2\theta = 24.2, 39.1, 44.8, 65.2, 77.8$ and are indexed as (100), (111), (200), (220), and (222) on matching with JCPDS card^[7]. It can be observed from the XRD spectrum of OPE-AgNPs that the peak corresponding to (111) plane has the highest intensity. This signifies that a large proportion of the nanoparticles exists in this orientation. Also, JPCD card matched the phase of silver to Ag⁰ indicating that the silver ions were actually reduced to zero valency which has been previously reported for other plant extracts mediated silver nanoparticles. Thus, the phytocompounds in orange peels extract act as reducing agent, reducing silver to zero valency while the silver ion acts as the oxidizing agent for the phytocompounds. With this scenario, the nanoparticles formed could be seen as resulting from capping of organic molecules of OPE on silver to form a coordinate covalently bonded complex which is organometallic in nature.

Average crystallite size (τ) of 62.6 nm was estimated from calculation using Scherrer's equation (Equation 3)^[8].

$$\tau = \frac{k\lambda}{\beta \cos \theta} \quad (3)$$

where k is the shape factor, β is the full width at half maximum (FWHM), λ is the X-ray wavelength and θ is the Bragg angle.

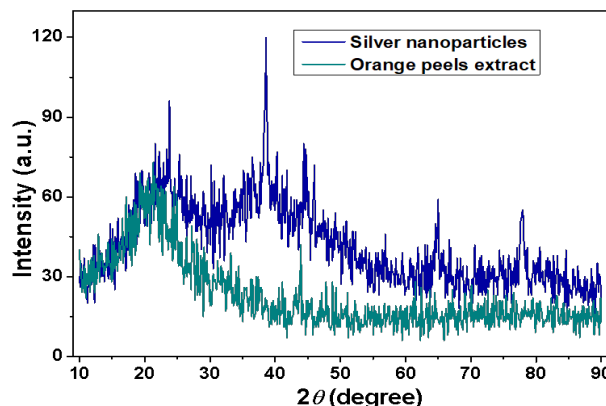


Figure 2. XRD diffraction pattern of Orange peels extract and the silver nano-powder.

The nanostructure, morphology and particle size of the nano-powder was determined by TEM and the image obtained is shown in Figure 3. It can be observed that nanoparticles were actually formed, and that the particles were almost uniformly round-shaped, non-agglomerated and around 55 nm in size. Particles with sizes range within 1 - 100 nm are usually considered to be nanoparticles^[9] and the average size of the synthesized material determined by TEM and XRD falls within this range.

3.2 Corrosion Measurement

The nano-powder was used as anticorrosion additive in the laboratory simulated scale dissolver liquor. The corrosion rate and inhibition efficiency obtained at different temperatures are presented in Table 1.

From the table, it can be observed that at all temperatures, corrosion rate was highest in the dissolver medium without the nano-powder. However, on addition of the nano-powder, corrosion rate reduces, indicating that corrosion has been inhibited. The inhibition efficiency increases as the concentration of the nano-powder increases but decreases on increase in temperature. The corrosion rate in the presence of the crude extract is higher than with the nano-powder, implying that the nanoparticles exhibit better anticorrosion effect than the crude extract.

At all temperatures and concentrations, the nano-powder yields higher inhibition efficiency than the extract implying that modification of the extract with silver nanoparticles improves its efficiency and resistance to

Table 1. Corrosion rate and inhibition efficiency in the presence and absence of OPE and nano-powder (NP) at various temperatures for 24 h immersion time

Test solution	30 °C		40 °C		50 °C		60 °C	
	$C_R(\text{mmpy})$	%I	$C_R(\text{mmpy})$	%I	$C_R(\text{mmpy})$	%I	$C_R(\text{mmpy})$	%I
1 M HCl	0.3845	-	0.7239	-	1.5440	-	2.2714	-
0.5 g/L OPE	0.0120	96.9	0.2992	58.7	0.7521	51.3	1.2102	46.7
0.10 g/L NP	0.0058	98.5	0.1564	78.4	0.4625	70.0	0.7365	67.6
0.30 g/L NP	0.0055	98.6	0.1164	83.9	0.3308	78.5	0.6098	73.2
0.50 g/L NP	0.0043	98.9	0.0926	87.2	0.2305	85.1	0.4275	81.2

thermal degradation^[10]. This inhibitive effect can be attributed to the adsorption of the nanoparticles on the surface of the X80 steel causing a 'barrier' for mass and charge transfer thus protecting the metal surface from corrosion. Adsorption can be by physical or chemical mechanism. As obtained in this study, where inhibition efficiency decreases with temperature increase, it can be implied that previously adsorbed molecules may have desorbed as temperature increases. This behaviour is consistent with physical adsorption mechanism.

3.3 Kinetic and Thermodynamic Studies

Most bio-based CIs act by adsorption of their phyto-compounds on active sites of the substrate (steel)^[11]. This occurs by adherence of their molecules on the substrate surface and is often driven by chemical or physical interactive forces. The nature of the force could be predicted by fitting surface coverage into various adsorption isotherm models as a function of concentration. However, the concentrations in this study are not in molar terms, hence adsorption isotherms could not be determined. Instead, linear plots that fit Arrhenius

equation (Equation 4) and thermodynamic transition state equation (Equation 5) were constructed as shown in Figure 3.

$$\log CR = \log A - \frac{E_a}{2.303RT} \quad (4)$$

$$\log\left(\frac{CR}{T}\right) = \left[\log\left(\frac{R}{Nh}\right) + \left(\frac{\Delta S^*}{2.303R}\right)\right] - \left(\frac{\Delta H^*}{2.303RT}\right) \quad (5)$$

where CR is the corrosion rate, N is Avogadro's number, R is the universal gas constant, h is Planck's constant, A the Arrhenius frequency constant, T is absolute temperature, ΔH^* and ΔS^* is the enthalpy and entropy change of activation, respectively.

Relevant activation parameters (Table 2) such as the apparent activation energy (E_a), enthalpy change (ΔH^*) and entropy change (ΔS^*) associated with the adsorption process were determined for all the test solutions. From results, E_a values were higher when both OPE and NPs were added than in the free acid solution. In the presence of the NPs especially, higher E_a values were obtained. This indicates that the additives increase the energy threshold for ease of corrosion. Thus, their adsorption elicited corrosion resistance on the substrate surface.

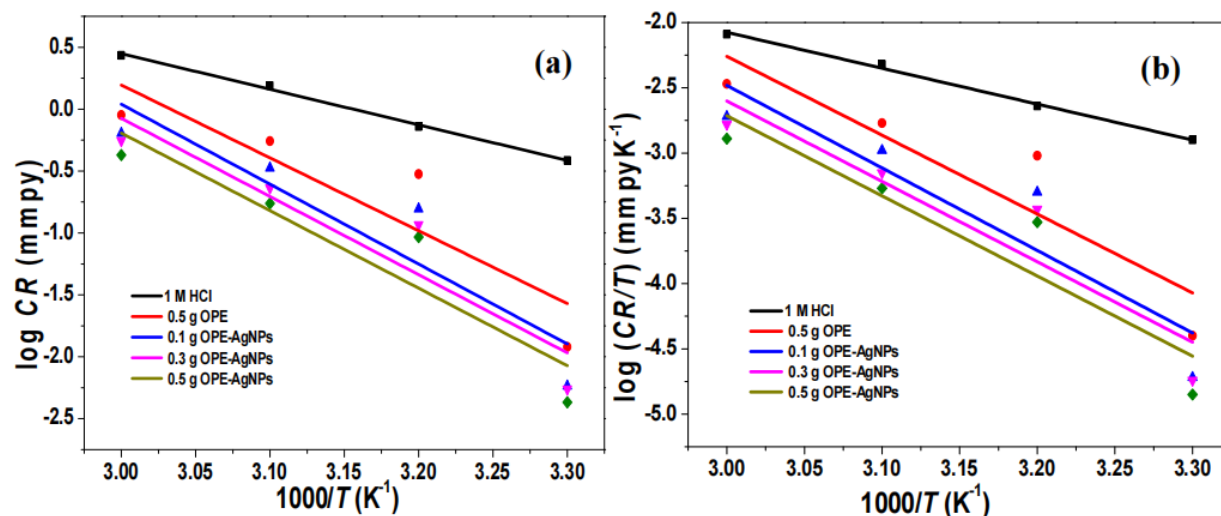


Figure 3. (a) Arrhenius plot and (b) Transition state plot for the corrosion of X80 steel in 1 M HCl containing OPE and the orange peel extract-silver nano-powders (OPE-AgNPs).

This resistance increases as concentration increases, a performance that has been associated physical adsorption mechanism in literature ^[12].

Table 2. Activation parameters obtained

Test solution	E_a (kJ/mol)	ΔH^* (kJ/mol)	ΔS^* (kJ/mol)
1 M HCl	21.31	-13.14	1.12
0.5 g/L OPE	28.47	-14.28	1.08
0.1 g/L OPE-AgNP	33.82	-16.42	0.94
0.3 g/L OPE-AgNP	41.75	-21.06	0.94
0.5 g/L OPE-AgNP	53.94	-25.88	0.87

Negative enthalpy changes were also obtained, which indicates that the adsorption was essentially exothermic, typical of physisorption mechanism ^[13]. The values of entropy change obtained were all positive and decreases in the presence of the additives in a concentration dependent manner. This indicates that the activated complex stage was dominated by association of molecules of inhibitor on the surface, rather than dissociation. Also, adsorption of the additives on the steel surface resulted in orderliness of the bulk solution ^[13].

4. Conclusions

The following conclusions are drawn based on empirical data:

- (1) Reaction between aqueous orange peels extract and silver nitrate produces nanofluid which can be dried to nano-powder.
- (2) Orange peels extract-silver nanopowder are round shaped, of 55 -63 nm average size and non agglomerating.
- (3) The nano-powders inhibit corrosion of X80 steel in simulated scale dissolver at 30 °C to 60 °C.
- (4) OPE-AgNPs inhibits corrosion better than the crude extract especially at high temperatures.

References

- [1] Rhudy, J. S. (1993). Removal of mineral scale from reservoir core by scale dissolver. In SPE International Symposium on Oilfield Chemistry. New Orleans, Louisiana, March 1993. SPE-25161-MS. <https://doi.org/10.2118/25161-MS>.
- [2] Fink, J. (2021). Petroleum engineer's guide to oil field chemicals and fluids. Gulf Professional Publishing.
- [3] Ituen, E., Akaranta, O. and James, A. (2016). Green anticorrosive oilfield chemicals from 5-hydroxytryptophan and synergistic additives for X80 steel surface protection in acidic well treatment fluids. *Journal of Molecular Liquids*, 224, 408-419.
- [4] Cicek, V. and Ozdemir, M. (2013). Characterization Studies Of Aqueous Immersion Solutions Of Novel Environmentally Friendly Organometallic Corrosion Inhibitors Used To Cure Mild Steel Substrates In Corrosive Media. *International Journal of Engineering Research and Application* 3(1), 1455-1461.
- [5] Singh, A., Dayu, X., Ituen, E., Ansari, K., Quraishi, M. A., Kaya, S. and Lin, Y. (2020). Tobacco extracted from the discarded cigarettes as an inhibitor of copper and zinc corrosion in an ASTM standard D1141-98 (2013) artificial seawater solution. *Journal of Materials Research and Technology*, 9(3), 5161-5173.
- [6] Ahmed, S., Ahmad, M., Swami, B. L. and Ikram, S. (2016). A review on plants extract mediated synthesis of silver nanoparticles for antimicrobial applications: a green expertise. *Journal of advanced research*, 7(1), 17-28.
- [7] Priyaragini, S., Sathishkumar, S. R., & Bhaskararao, K. V. (2013). Biosynthesis of silver nanoparticles using actinobacteria and evaluating its antimicrobial and cytotoxicity activity. *International Journal of Pharmaceutical Science*. 5(2), 709-712.
- [8] Ituen, E., Yuanhua, L., Verma, C., Alfantazi, A., Akaranta, O. and Ebenso, E. E. (2021). Synthesis and characterization of walnut husk extract-silver nanocomposites for removal of heavy metals from petroleum wastewater and its consequences on pipework steel corrosion. *Journal of Molecular Liquids*, 335, 116132.
- [9] Domingos, R. F., Baalousha, M. A., Ju-Nam, Y., Reid, M. M., Tufenkji, N., Lead, J. R., Leppard, G. G. and Wilkinson, K. J. (2009). Characterizing manufactured nanoparticles in the environment: multimethod determination of particle sizes. *Environmental Science and Technology*, 43(19), 7277-7284.
- [10] Ituen, E., Singh, A., Yuanhua, L. and Akaranta, O. (2021). Green synthesis and anticorrosion effect of Allium cepa peels extract-silver nanoparticles composite in simulated oilfield pickling solution. *SN Applied Sciences*, 3(6), 1-17.
- [11] Ituen, E., Akaranta, O. and James, A. (2017). Evaluation of performance of corrosion inhibitors using adsorption isotherm models: an overview. *Chemical Science International Journal*. 18(1), 1-34.
- [12] Faraj, N., Abdelghani, K. A., Idress, A. A. and Ibrahim, D. M. (2021). L-Proline as a Green Corrosion Inhibitor in Aqueous Solutions for Carbon Steel. *Journal of Metallic Material Research*, 4(1), 16 -20.
- [13] Chidiebere, M. A., Oguzie, E. E., Liu, L., Li, Y. and Wang, F. (2014). Corrosion inhibition of Q235 mild steel in 0.5 M H₂SO₄ solution by phytic acid and synergistic iodide additives. *Industrial and Engineering Chemistry Research*, 53(18), 7670-7679.

Journal of Metallic Material Research

Aims and Scope

Journal of Metallic Material Research is a peer-reviewed, open-access journal dedicated to the research of metallic materials. As a critical component of the human civilization, metal has been infused into many aspects of our lives. The journal is focused on innovations in the research of metallic materials.

The scope of the Journal of Metallic Material Research includes, but is not limited to:

- Properties of metallic materials (Physical/Mechanical/Electrical/Chemical)
- Functions of metallic materials
- Applications of metallic materials
- Alloys
- Recycling

Bilingual Publishing Co. (BPC)

Tel: +65 65881289

E-mail: contact@bilpublishing.com

Website: www.bilpublishing.com

About the Publisher

Bilingual Publishing Co. (BPC) is an international publisher of online, open access and scholarly peer-reviewed journals covering a wide range of academic disciplines including science, technology, medicine, engineering, education and social science. Reflecting the latest research from a broad sweep of subjects, our content is accessible world-wide—both in print and online.

BPC aims to provide an analytics as well as platform for information exchange and discussion that help organizations and professionals in advancing society for the betterment of mankind. BPC hopes to be indexed by well-known databases in order to expand its reach to the science community, and eventually grow to be a reputable publisher recognized by scholars and researchers around the world.

BPC adopts the Open Journal Systems, see on ojs.bilpublishing.com

Database Inclusion



Asia & Pacific Science
Citation Index



Creative Commons



China National Knowledge
Infrastructure



Google Scholar



Crossref



MyScienceWork

